

# Transition-Edge Sensors for cryogenic X-ray imaging spectrometers

Luciano Gottardi\* and Stephen Smith

**Abstract** Large arrays of superconducting transition-edge sensor (TES) microcalorimeters are becoming the key technology for future space-based X-ray observatories and ground-based experiments in the fields of astrophysics, laboratory astrophysics, plasma physics, particle physics and material analysis. Thanks to their sharp superconducting-to-normal transition, TESs can achieve very high sensitivity in detecting small temperature changes at very low temperature. TES based X-ray detectors are non-dispersive spectrometers bringing together high resolving power, imaging capability and high-quantum efficiency simultaneously. In this chapter, we highlight the basic principles behind the operation and design of TESs, and their fundamental noise limits. We will further elaborate on the key fundamental physics processes that guide the design and optimization of the detector. We will then describe pulse-processing and important calibration considerations for space flight instruments, before introducing novel multi-pixel TES designs and discussing applications in future X-ray space missions over the coming decades.

## Keywords

**Key words:** Imaging spectroscopy, transition-edge sensor, microcalorimeter array, superconductivity, weak-link, X-ray astrophysics, laboratory astrophysics.

---

Luciano Gottardi

NWO-I/SRON Netherlands Institute for Space Research, Niels Bohrweg 4, 2333CA Leiden, The Netherlands. e-mail: [l.gottardi@sron.nl](mailto:l.gottardi@sron.nl)

Stephen Smith

NASA Goddard Space Flight Center, 8800 Greenbelt Road, Greenbelt, MD 20771, USA e-mail: [stephen.j.smith@nasa.gov](mailto:stephen.j.smith@nasa.gov)

\* corresponding author



# Contents

<b>Transition-Edge Sensors for cryogenic X-ray imaging spectrometers</b> .....	<b>1</b>
Luciano Gottardi and Stephen Smith	
Keywords .....	1
Introduction .....	3
Theoretical and Experimental Background .....	4
Basic Principles .....	4
TES Electrical and Thermal Response .....	6
Negative Electrothermal Feedback .....	7
Fundamental Noise Sources .....	8
Non-linearity .....	10
Pulse Processing .....	11
Detector Design .....	13
TES Properties .....	13
Thermal Isolation .....	14
Absorber Design and Properties .....	14
Current State of the Art .....	15
Physics of the Superconducting Transition .....	16
The Superconducting Transition .....	16
Josephson Effects in DC and AC Biased TESs .....	18
Implication of the Weak-Link Behaviour on the Detector Noise .....	22
Detector Calibration Considerations .....	22
Response Function .....	23
Energy Scale and Sensitivity to Environmental Fluctuations .....	24
Drift Correction Algorithms .....	26
Multi-Pixel TESs .....	26
Applications and Future Technology Needs .....	28
Ground Based Instrumentation .....	28
Next Generation Space Mission Concepts .....	29
References .....	32

## Introduction

X-ray spectroscopy provides an excellent diagnostic probe of the energetics and physical conditions in nearly all classes of cosmic objects throughout the observable universe. X-rays are emitted by various high-energy processes. By observing their spectra we can obtain information about the temperature, electron density and ionic composition of hot plasma's, and answer many questions across astrophysics (from

understanding turbulence in galaxy clusters to the accretion processes in binary systems or active galactic nuclei.)

Microcalorimeters are non-dispersive thermal detectors that will provide the next major step in imaging spectroscopy capabilities compared to gas proportional counters or charge coupled devices (CCD) which have been extensively used in X-ray space instrumentation over the past several decades. Microcalorimeters will full-fill the needs of X-ray astrophysics in the 21st century, combining eV level energy resolution in the soft X-ray energy range in large format imaging arrays with potentially 1000's of pixels. With resolving powers  $> 1000$ , microcalorimeters are competitive with dispersive grating spectrometers, but with the advantage of high collection efficiency. This enables efficient observations of point sources and extended sources with the same instrument. The sensor technology used in microcalorimeters can come in different forms - silicon thermistors, transition-edge sensors (TESs) and magnetic microcalorimeters (MMCs) - but the basic principle is the same. A microcalorimeter measures the temperature rise resulting from the energy deposited by a single X-ray photon. The sensor transduces the change in temperature to an electrical signal (either through a resistance change for thermistors and TESs or a change in magnetism for MMCs), from which the photon energy can then be determined. In order to achieve resolving powers of  $\sim 1000$ 's at keV energies, extremely low detector noise is required, only achievable when operating at mK temperatures. The potential power of microcalorimeters to revolutionize X-ray astrophysics has already been demonstrated by the observation of the Perseus galaxy cluster by the Hitomi satellite's Soft X-ray Imaging Spectrometer (SXS) [63].

In this chapter, we describe microcalorimeters based around highly sensitive transition-edge-sensors (TESs). TESs are next generation microcalorimeters based on a thin superconducting film that is electrically biased in the narrow region between superconducting (zero-resistance) state and the normal resistive state. The transition region is typically only a few mK in width and as such, TES detectors are extremely sensitive to temperature changes making them ideal detectors for high resolution X-ray spectroscopy. We start by outlining the basic principles behind the operation and design of TESs, and their fundamental noise limits. We will elaborate on the key fundamental physics effects that guide the design and optimization of the TESs. We will then describe important calibration considerations for space flight instruments. We will continue by introducing novel multi-pixel TES designs and conclude the chapter by presenting the applications in future X-ray space missions over the coming decades.

## Theoretical and Experimental Background

### *Basic Principles*

A TES-based X-ray detector is a thermal equilibrium calorimeter. It consists of three fundamental components: an absorber with heat capacity  $C$ , a thermometer (the TES), and a weak thermal link, with a conductivity  $G_{bath}$ , to the heat sink at temperature  $T_{bath}$ , which is below the operating temperature of the device. Details on the design of each of these components is described in Section . A simplified scheme of a TES calorimeter is shown in Fig. (1).

TESs are based on superconducting thin films, voltage biased in the narrow transition region between the onset of resistance and the fully normal state. A single photon deposits its energy  $E$  into the absorber, which converts it into heat. The temperature rise, proportional to the energy, causes a change in resistance of the TES. The resistance change is determined by monitoring the current through the TES using a superconducting quantum interference device (SQUID) ammeter. Within this general description, there is room for countless variations. Important device parameters such as the noise,  $G_{bath}$  and  $C$  are strongly dependent on the operating temperature of the device. Thus, the transition temperature of the TES must be chosen to achieve the desired energy resolution and response time, whilst being compatible with the instrument cryogenic architecture. For typical astrophysics applications a transition temperature of below 100 mK is ideal.

Thermal equilibrium detectors can achieve excellent energy resolution. A fundamental limit for the minimum energy resolution  $\Delta E$  offered by a calorimeter is given by the random exchange of energy between the detector and the thermal bath [105]. This thermodynamic limit is given by  $\langle \Delta E_{TD}^2 \rangle = k_B T^2 C$ . It depends quadratically on the temperature  $T$  of the calorimeter, linearly on the detector heat capacity  $C$ , and it is independent on the thermal conductance  $G_{bath}$  of the thermal link.

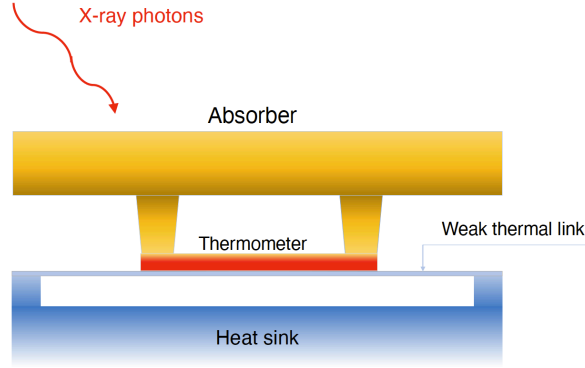


**Fig. 1** Schematic of a TES-based X-ray microcalorimeter. The TES is a very sensitive thermometer that detects the temperature rise from the energy deposited in the absorber by an X-ray photon.

The ultimate sensitivity of a TES microcalorimeter depends on the shape of the TES superconducting-to-normal transition and the intrinsic noise sources of the detector and the read-out circuit. The resistance,  $R(T, I)$ , of a TES is generally a function of both the temperature of the device,  $T$ , and the current flowing through it,  $I$ . For small changes about the equilibrium bias conditions  $(R_0, T_0, I_0)$  the device resistance can be expressed as

$$R(T, I) \simeq R_0 + \alpha \frac{R_0}{T_0} \delta T + \beta \frac{R_0}{I_0} \delta I. \quad (1)$$

The two dimensionless parameters  $\alpha = \partial \log R / \partial \log T$  and  $\beta = \partial \log R / \partial \log I$ , calculated at a constant current and temperature respectively, are conveniently used to parameterize the current and temperature sensitivity of the resistive transition at the operating point [94].

The energy resolution of an ideal TES calorimeter, limited only by the fundamental thermal fluctuations due to the exchange of energy between the calorimeter and the thermal bath, is given by [105]

$$\Delta E \propto \sqrt{4k_B T_0^2 \frac{C}{\alpha}}, \quad (2)$$

where the logarithmic derivative of resistance  $\alpha$ , introduced above, describes the steepness of the superconducting transition. By developing TESs with a large temperature sensitivity  $\alpha$ , the photon energy can be measured with a much higher resolution than the magnitude set by thermodynamic fluctuations. Eq. (2) tells us that low heat capacity devices, operating at very low temperature  $T_0$ , could achieve very high energy resolution. However, the value of  $C, \alpha$  and  $T_0$  are constrained by the maximum energy to be detected. For high energetic photons, the temperature excursion could be so high to drive the TES in the normal state and to saturate the detector. The saturation energy  $E_{sat}$  is proportional to  $E_{sat} \propto C/\alpha$ , which effectively means that the theoretical energy resolution  $\Delta E \propto \sqrt{E_{sat}}$ .

A detail analysis of the noise, the electrothermal response and the ultimate sensitivity of a TES microcalorimeter will be presented in the following sections.

## TES Electrical and Thermal Response

A TES detector can be electrically voltage biased in its transition region using either an AC or DC voltage biasing scheme. Although the design of the electrical bias circuit is naturally different for the two approaches, the resulting electrothermal behaviour of the TES is generally equivalent. Whether a TES is AC or DC biased can, however, affect the transition shape and noise properties of the device and may lead to different optimal pixel designs [55].

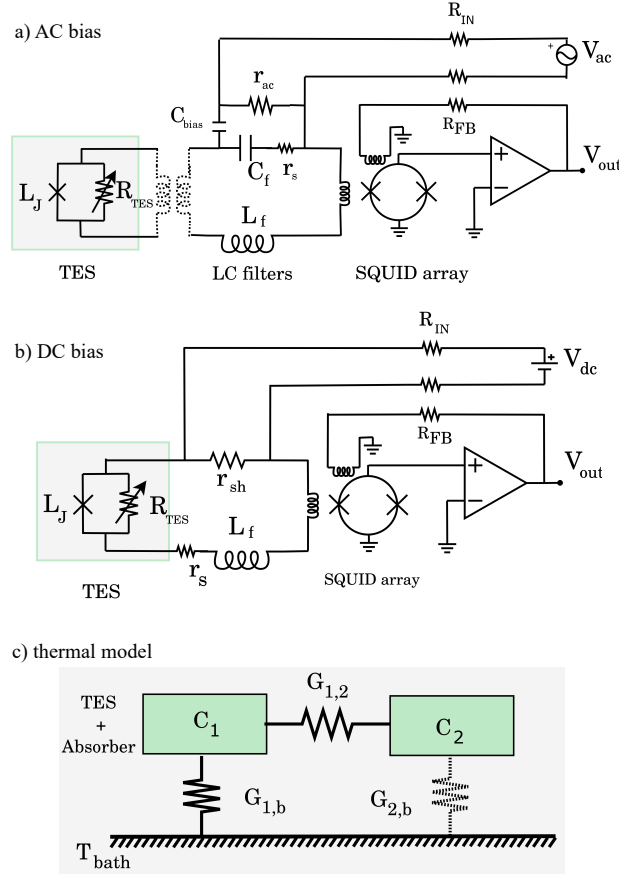


**Fig. 2** a) AC bias electrical circuit, b) DC bias electrical circuit, c) Example of a two-body thermal model with two heat capacitance  $C_1$  and  $C_2$ , linked by a thermal conductance  $G_{12}$ , and with parallel connection to the heat sink,  $G_{1,b}$  and  $G_{2,b}$ , defining the total thermal conductance to the bath,  $G_{bath}$ .

A schematic diagram of the AC and DC bias read-out circuit and the detector thermal model are shown in Fig. (2). The fundamental difference between the two bias configurations is that, in the AC bias case, the TES is brought into transition by the rms power generated by an alternating voltage at few MHz frequency, while in the DC bias case a constant voltage is applied.

Under AC bias the TES is placed in series with a high- $Q$  superconducting LC filter [22, 23] and the input coil of the SQUID current amplifier [80]. An optional superconducting transformer, shown in the picture in dashed lines, could be used to optimize the impedance matching between detector and amplifier. The AC voltage bias, tuned at the LC filter resonant frequency  $f_{bias} = f_{LC} = 1/(2\pi\sqrt{LC})$ , is provided via a capacitive divider in parallel with an AC shunt resistor. From a simple Thevenin equivalent circuit analysis, the bias network is equivalent to a shunt resistance  $r_{sh} \simeq r_{ac}C_b/(C_f + C_b) + r_s$ , in series with the LC resonator, where  $r_s$  accounts for the intrinsic loss in the LC-filters [59]. The DC bias circuit is shown in Fig. (2)b. where  $L_f$  is the Nyquist inductor added to limit the read-out bandwidth,  $r_{sh}$  is a low ohmic shunt

resistors needed to provide a stiff dc voltage bias to the TES, and  $r_s$  indicates any parasitic resistance in the bias circuit. Both for the AC and DC read-out the following should hold:  $r_s \ll r_{sh} \ll R_N$ . The standard electrothermal linear model that describes the noise and the small signal response to photons of a DC biased TES calorimeter has been extensively presented and analysed in the literature [70, 94]. The formalism for the AC biased case was first reported by van der Kuur, J. et al. in [86]. In this model, the TES resistance is linearly approximated as in Eq. (1) with no assumptions made on the physical phenomena occurring at the superconducting transition. This simplified model has been successfully used to understand the behaviour of TES-based detectors in many works that followed. As observed in many experiments [53, 78, 102, 150, 160], due to the presence of parasitic heat capacitance and a limited thermal conductance in the TES-absorber structures, a single-body thermal model for a TES calorimeter is not always sufficient to explain the detector thermal response. It can be shown that a two-body model, as drawn in Fig. (2)c with two heat capacitance  $C_1$  and  $C_2$  linked by a thermal conductance  $G_{12}$ , is sufficiently general to account for parasitic thermal effects in TES-based detectors. The heat capacity  $C_1$  is typically the sum of the TES bilayer and the absorber heat capacity, since the two structures are generally thermally well coupled, while  $C_2$  is a potential decoupled heat capacitance which could have different physical sources, like a fraction of the TES bilayer, the supporting  $Si_xN_y$  membrane, or the leads [53, 96, 150, 160]. A more detailed analysis for even more complex thermal structures can be found for example in [78, 102]. One has to keep in mind, however, that the model could be unconstrained when too many thermal bodies are added into the system of equations. As a consequence, the physical interpretation of the results becomes impossible.

The detector response is regulated by the Joule power provided by the bias circuit,  $P_J = V_{TES}^2/R_{TES}$  and the power  $P_{bath}$  flowing to the thermal bath, given by

$$P_{bath} = k(T^n - T_{bath}^n), \quad (3)$$

where  $k = G_{bath}/n(T^{n-1})$ , with  $G_{bath}$  the differential thermal conductance to the thermal bath,  $n$  the thermal conductance exponent, and  $T_{bath}$  the bath temperature [70]. The parameters  $n$  and  $K$  are material and geometry dependent parameters that depend on the design of the physical link to the heat bath (see Section ). The system is characterized by two fundamental time constants,  $\tau = C/G_{bath}$  and  $\tau_{el} = \frac{L}{r_{sh} + R_0(1+\beta)}$ , defining respectively the thermal and electrical bandwidth.

The Langevin electrothermal equations for a TES calorimeter, generalized for the DC and AC biased case have been extensively studied in the literature [55, 70, 96, 155, 160]. The system of coupled non-linear differential electrothermal equations is typically solved in the small signal regime and in the linear approximation. In this case, the detector physics is generally ignored and  $R(T, I)$  is parametrized as in Eq. (1) [70, 86, 94, 96, 151]. For this system of coupled linear differential equations there exist analytical solutions, which are either over-, under-, or critically damped. The stability criteria is discussed in the following section.

As it will be shown in Section , many of the physical phenomena observed at the TES transition can be explained in the framework of the weak-superconductivity. The detector physics can then be formally included in the electrothermal equations as shown in [55]. They have been fully solved numerically, for an AC biased pixel, in the simplified single-thermal body case [79]. This numerical time-domain model can be used to simulate the TES response to the incoming photons in the non-linear and large signal regime, as it is done for example in the end-to-end simulator under development for the X-IFU on Athena [99, 168].

## ***Negative Electrothermal Feedback***

The thermal and electrical circuits of a TES are coupled via the cross-terms in the thermal-electrical differential equations [55]. A temperature change in the TES leads to an electrical current signal as a result of a change in the TES resistance. Under voltage-bias conditions ( $r_{sh} \ll R(T_0, I_0)$ ), the electrical current signal change is restored by a change of the Joule power,  $P_J = V_{TES}^2/R(T_0, I_0)$ , which decreases with increasing temperature. This process is analogous to the electrical feedback in a transistor circuit. It involves both the electrical and the thermal circuits simultaneously, and it has been named, for this reason, electrothermal feedback (ETF). In the voltage bias case, the ETF is negative and the TES is stable against thermal run-

away. The zero frequency ETF loop gain  $\mathcal{L}_0$  depends on the detector intrinsic quiescent parameters such as  $\alpha$ ,  $G_{bath}$ ,  $P_0 = I_0^2 R_0$ ,  $T_0$  and the bias circuit shunt resistor  $r_{sh}$ , and it is defined as

$$\mathcal{L}_0 = \alpha \frac{1 - r_{sh}/R(T_0, I_0)}{1 + r_{sh}/R(T_0, I_0) + \beta} \frac{I_0^2 R_0}{T_0 G_{bath}}. \quad (4)$$

For a constant current,  $\beta = 0$ , and in the limit of  $R(T, I) \gg r_{sh}$ , the loop gain  $\mathcal{L}_0$  reduces to the standard loop gain  $\mathcal{L}_I = \alpha \frac{I_0^2 R_0}{T_0 G_{bath}}$  found in the literature [70].

As it is the case for transistors, there are significant advantages in operating a TES in the negative EFT mode, such as reduced sensitivity to TES parameter variation, faster response time, increased linearity and dynamic range, self-biasing, and self-calibration. [70, 71]. As any feedback scheme, ETF can become unstable depending on the detector and the bias circuit parameters. The stability criteria for a TES microcalorimeter have been extensively discussed by Irwin [70, 71]. For a single thermal body, the stability condition for the solution of the system is met for positive values of the real part of the eigenvalues  $1/\tau_+$  and  $1/\tau_-$  derived in [70], where  $\tau_+$  and  $\tau_-$  are defined as the rise-time and fall-time of a pulse generated by a X-ray photon absorbed by the detector.

In the limit of a small electrical inductance  $L$ , the rise-time  $\tau_+$  reduces to the electrical circuit time constant  $\tau_{el}$ , while the effective thermal time constant of the TES becomes

$$\tau_{eff} = \tau_-|_{L=0} = \frac{C}{G_{bath}} \frac{1 + \beta + r_{sh}/R(T_0, I_0)}{1 + \beta + r_{sh}/R(T_0, I_0) + (1 - r_{sh}/R(T_0, I_0))\mathcal{L}_I}. \quad (5)$$

In the stiff voltage bias limit ( $r_{sh} \ll R_0$ ), we get

$$\tau_{eff} = \frac{C}{G} \frac{1 + \beta}{1 + \beta + \mathcal{L}_I}. \quad (6)$$

The equations above show that the relaxation time to the steady state after a photon absorption is reduced by the ETF loop gain  $\mathcal{L}_I$ . Furthermore, the thermal time constant of the detector is directly proportional to the  $\alpha$  and  $\beta$  parameters, and therefore depends significantly on the local properties of the transition.

The condition on the time constants  $\tau_{\pm}$  being real for a stable, critically ( $\tau_+ = \tau_-$ ) or overdamped ( $\tau_+ < \tau_-$ ) detector response reduces to a constrain on the inductance  $L$  of the bias circuit. For given bias conditions and intrinsic TES properties, the system is underdamped for  $L_{crit-} < L < L_{crit+}$  and the detector shows an oscillating response. The critical inductance  $L_{crit\pm}$  is defined in [70]. Typically, the TES calorimeter readout circuit is dimensioned such that the electrical circuit is faster than the thermal circuit with  $L \leq L_{crit-}$  where the best temperature-to-current responsivity is achieved. In the limit of strong voltage bias  $r_{sh} \ll R_0$  and high feedback gain  $\mathcal{L}_0 \gg 1, \beta$ , the critical inductance  $L_{crit\pm}$  reduces to

$$L_{crit\pm} \simeq \frac{CT_0 R_0}{P_0} \left( \frac{3 + \beta \pm 2\sqrt{2 + \beta}}{\alpha} \right), \quad (7)$$

which is defined solely by the TES calorimeter physical parameters.

The form of the stability space is more complicated when a two-body thermal body is present [12] or when the magnetic field dependence of the resistive transition needs to be included [125] and a more careful analysis is required.

The effect of the inductance  $L$  of the electrical bias circuit on the detector linearity in the small and large signal limit is further discussed in Section and shown in Fig. (4).

## Fundamental Noise Sources

Noise sources in a TES-based microcalorimeter can be placed into three categories: (1) noise sources internal to the TES, (2) noise sources from the circuit in which the TES is embedded, such as Johnson noise in the bias resistor and the noise contribution of the readout amplifier, and (3) noise from the external environ-



ment such as magnetic field, RF-pickup, stray photon arrivals, and fluctuations in the temperature bath. The read-out amplification chain is typically dimensioned to give a negligible noise contribution on the detector performance, while the noise from the external environment is generally minimized by a proper design of the focal plane assembly. The major intrinsic noise sources in a TES calorimeter originate from the thermal fluctuations in the phonon and electronic ensemble of the device. Three intrinsic noise contributions are generally identified: the phonon noise, the internal thermal fluctuation noise and the Johnson-Nyquist noise. As an example, we show in Fig. (3), the typical current noise spectrum of a TES calorimeter under AC bias [61].

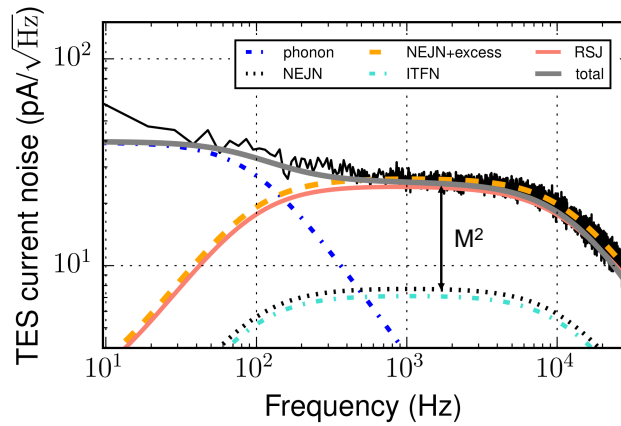


**Fig. 3** Example of a current noise spectrum for a TiAu  $80 \times 20 \mu\text{m}^2$  TES AC biased at 2.6 MHz,  $R/R_N = 13\%$  and  $T_{bath} = 55$  mK. The different lines show the noise contributions discussed in the text. The vertical arrow indicates the measured excess noise with respect to the estimated non-equilibrium Johnson noise (NEJN). The red solid line is the prediction of the Johnson noise based on the resistively shunted junction model. Reproduced from [61].

The *phonon noise*, blue dot-dashed line in Fig. (3), arises from the statistical energy fluctuations generated during the random energy exchange between the TES-absorber body and the heat bath. The power spectral density of this noise is  $S_{ph} = 4k_B T^2 G_{bath} F(T_0, T_{bath})$ , where  $G_{bath}$  is the thermal conductance to the bath at a temperature  $T_{bath}$ . For thermal transport where the mean free path of the energy carriers is larger than the length of the link (radiative transport),  $F(T_0, T_{bath}) = ((T_{bath}/T)^{n+2} + 1)/2 \sim 0.5$ , [19], with  $n$  the thermal-process dependent exponent. This noise is dominant at low frequencies in the detector thermal bandwidth typically below  $\sim 200$ Hz.

The *internal thermal fluctuation noise* (ITFN), cyan dot-dashed line, is generated by thermal fluctuation between distributed heat capacities internal to the TES-absorber, as for example in the two-body model shown in Fig. (2). It has a power spectral density  $S_{itfn} = 4k_B T^2 G_{12}$ , where  $G_{12}$  is the thermal conductance between the two thermal bodies. The ITFN contribution can be derived from a proper characterization of the thermal circuit [34, 64, 78, 102, 150, 160, 161].

The third main contribution to the TES total noise is the *Johnson-Nyquist noise* (JN) of the TES biased in the resistive transition. It can be written in the form of a voltage noise  $e_{int} = \sqrt{4k_B T R \zeta(I)}$ . The response of the TES current to  $e_{int}$  is suppressed at low frequency by the electrothermal feedback [71] and becomes significant in the detector electrical band at kHz. The function  $\zeta(I)$ , which is strongly dependent on the TES current, conveniently describes the noise originated from the non-linear TES resistance nearly at equilibrium at the quiescent temperature  $T_0$ . It takes into account the non-linear correction terms to the linear equilibrium Johnson noise. For a linear resistance,  $\zeta(I) = 1$ . For a TES, the form of  $\zeta(I)$  is not straightforward to model due to the non-linear and non-equilibrium physical processes involved. The characterization of the noise in the electrical bandwidth is complicated by the fact that both the Nyquist-Johnson noise and the internal thermal fluctuation noise give a similar contribution in the measured TES current noise, after passing through the system transadmittance [102, 159, 160]. To calculate  $\zeta(I)$ , Irwin [69] assumed the TES to be a simple Markovian system with no hidden variables such as internal temperature gradients and fluctuating

current paths. By applying the Stratonovich's nonequilibrium Markovian fluctuation–dissipation relations, he calculated the first order, near-equilibrium, non-linear correction term to the noise to be  $\zeta_{ne}(I) = 1 + 2\beta$  [69].

In this form, the noise model is known as the non-equilibrium Johnson noise and it is extensively used in the literature to model the,  $\beta$  dependent, Nyquist–Johnson voltage noise observed in the TES. However, the broadband noise, typically observed in the TES electrical bandwidth [154], could only partially be explained after the introduction of the correction term  $\zeta_{ne}(I)$  and only at relatively low  $\beta$  values [75, 133, 150]. Smith et al. [133], for example, observed unexplained noise at high frequency after excluding the presence of a significant contribution of the ITFN in their data taken with low resistance, large  $\beta$ , high thermal conductance devices.

New experimental results on the noise characterization of TES microcalorimeter [61, 166] indicate that the observed Nyquist–Johnson voltage could find a theoretical explanation in the framework of the Josephson effects in the superconducting film described in Section . Due to the non-linear current–to-voltage relationship of the TES, the thermal fluctuation noise of the oscillating current induced at the Josephson frequency, much higher than the detector bandwidth, is mixed down and leads to an increase of noise in the TES electrical bandwidth (red solid line labelled RSJ in Fig. (3)). This noise mechanism will be discussed further in Section .

A detailed analysis of the thermometer sensitivity, the detector noise and the signal bandwidth, shows that the minimum energy resolution achievable with a TES calorimeter can be written as

$$\Delta E_{FWHM} \simeq 2\sqrt{2\ln 2} \sqrt{4k_B T_0^2 C \frac{\sqrt{\zeta(I)}}{\alpha} \sqrt{\frac{nF(T_0, T_{bath})}{1 - (T_{bath}/T_0)^n}}}. \quad (8)$$

The unit-less parameter  $F(T_0, T_{bath})$  and the thermal conductance exponent  $n$  depend on the physical nature of the thermal conductance and whether, for example, the phonon transport from the TES to the heat sink is radiative or diffusive [105]. For a TES,  $F(T_0, T_{bath}) \simeq 0.5$  and  $n \simeq 3$  [70]. To achieve the ultimate sensitivity, for given  $C$  and  $T_0$ , the factor  $\sqrt{\zeta(I)}/\alpha$  has to be minimized.

## Non-linearity

The equations and discussion outlined in Section to describe the TES behaviour in the small signal limit. This assumes the TES response as a function of photon energy is purely linear. TESs however, are generally non-linear devices and the pulse shapes (and noise properties during the pulse) will vary depending upon the deposited energy. Non-linearity comes about from two basic effects. Firstly, the shape of the resistive transition  $R(T, I)$  is inherently non-linear (see for example Fig. (9)). The temperature increase of the TES is proportional to the photon energy ( $\Delta T = E/C$ ). The larger the  $\Delta T$ , the closer the TES resistance is driven towards the normal branch of the transition and eventually the response of the TES will saturate as  $R_0 + \Delta R \rightarrow R_n$ . Secondly, even for a linear resistive transition (constant  $dR/dT$  and  $dR/dI$ ), non-linearity occurs due to the voltage biased nature of the electrical bias circuit itself. The maximum current change from the X-ray event  $\Delta I$  is constrained by the TES equilibrium bias current  $I_0$ , thus the current response will gradually saturate as  $\Delta I \rightarrow I_0$ . The TES current scales roughly as  $1/R$ , thus for every doubling of  $\Delta R$ , the corresponding  $\Delta I$  will be reduced by a factor of 2. The current and resistance non-linearity will both contribute to the large signal behaviour of TES detectors. Non-linearity not only affects the pulse shapes, but it also changes the intrinsic detector noise during the X-ray pulse. Generally, as the resistance increases the total detector noise will decrease, this can have a beneficial effect of compensating for the decreased amplitude of the pulse shape due to the non-linearity. The combined effect on the energy resolution is dependent upon the pulse processing method, the details of which will be discussed in Section .

Multiplexed readout schemes such as time-division-multiplexing (TDM) and frequency-domain-multiplexing (FDM) only have a finite available bandwidth (see Chapter "Signal readout for Transition-Edge Sensor X-ray imaging spectrometers" for a detailed discussion on these readout schemes). In order to optimally match the bandwidth of the detectors to the readout, a circuit inductance  $L$  is typically chosen to critically damp

the detector response. In the small signal limit, adding circuit inductance changes the detector responsivity, but does not affect the fundamental energy resolution (the signal and noise are affected equally). However it is interesting to consider that the increase in inductance can affect the detector linearity in the larger signal limit.

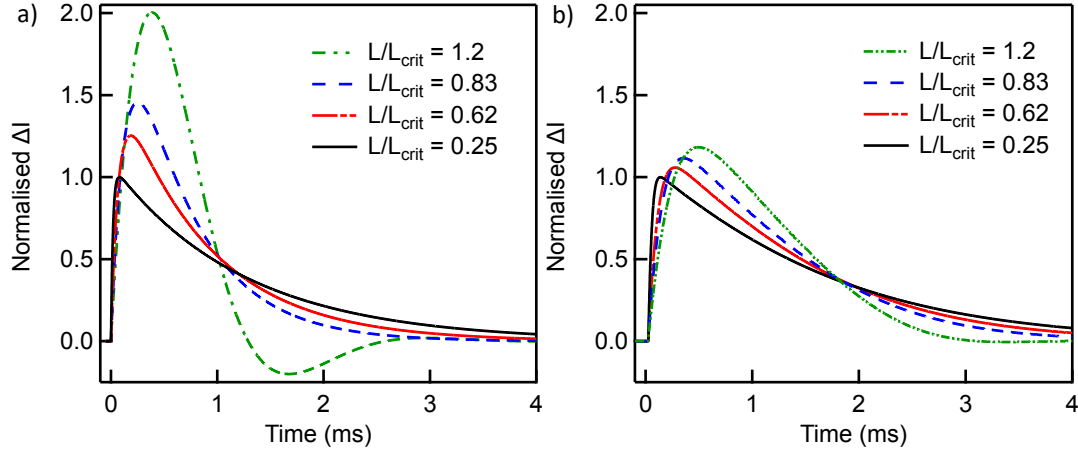


**Fig. 4** (a) Small signal modelled pulse shapes as a function of  $L/L_{crit}$ . (b) Measured pulse shapes at 6 keV as a function of  $L/L_{crit}$ . Data are normalized to the peak of the low inductance pulse-height in both cases. These data show how the small signal pulse height is strongly affected by  $L/L_{crit}$ , whereas due to the effects on non-linearity the measured large signal data shows only a modest increase in pulse-height.

Fig. (4) a) shows the small signal modelled pulse shapes as a function of  $L/L_{crit}$  for an Athena/X-IFU pixel compared to b) the measured pulse shapes at 6 keV as a function of  $L/L_{crit}$  [143]. Data are normalized to the peak of the low inductance pulse-height in both cases. These data show how the small signal (linear) modelled pulse shape is strongly affected by  $L/L_{crit}$ . The TES response is not limited by either current or resistance non-linearity, and the pulses become larger and faster as  $L/L_{crit}$  is increased. Whereas for the real device, which has a non-linear response to 6 keV X-rays, the measured large signal data shows only a modest increase in pulse-height with increasing  $L/L_{crit}$ . This is because the inherent non-linear response of the real device suppresses the increased current and resistance changes predicted from the small signal model. Thus the current response of the real device becomes increasing more nonlinear as a function of energy, with increasing  $L/L_{crit}$ . Significant non-linearity may impact the achievable resolution of the device and complicate the energy scale calibration. Thus for some device designs and applications it may be preferable to operate below the small signal critically damped limit of  $L/L_{crit} = 1$ .

### Pulse Processing

The output signal of a TES calorimeter is typically the amplified and digitised change in the TES current. The time stream of the detector output is sampled into records of a fixed length, which can be represented as a vector  $\mathbf{S}$ . In the small signal limit, and for records containing only a single X-ray pulse of energy  $E_k$ , the signal is proportional to the energy  $\mathbf{S} = E_k \mathbf{T}_k + \mathbf{n}$ , where  $\mathbf{T}_k$  is the noise-free signal and  $\mathbf{n}$  is the stationary additive noise from the detector and electronics. The best estimate of  $E_k$ , when the noise is not-white, would be given by minimising, with respect to  $E_k \mathbf{T}_k$ , the  $\chi^2$ :

$$\chi_k^2 = (\mathbf{S} - E_k \mathbf{T}_k)^T \mathbf{W} (\mathbf{S} - E_k \mathbf{T}_k), \quad (9)$$

being  $\mathbf{W} = \mathbf{N}^{-1}$ , the inverse of the noise variance-covariance matrix, where the diagonal elements are the variances,  $N_{ii} = \sigma_i^2$  and the off-diagonal elements are the covariances,  $A_{ij} = \sigma_{ij}$  from the noise sources. This leads to the following definition for the pulse energy

$$E_k = \mathbf{S}^T \begin{bmatrix} \mathbf{W}\mathbf{T}_k \\ \mathbf{T}_k^T \mathbf{W}\mathbf{T}_k \end{bmatrix} = \mathbf{S}^T \mathbf{F}, \quad (10)$$

where  $\mathbf{F}$  is the optimal filter. First introduced by Szymkowiak et al. (1993) [146], the optimal filtering technique has been used routinely in the analysis of X-ray micro-calorimeter pulses in laboratory experiments [46, 47, 167] and on space satellites [18, 130, 153].

In practice, the optimal filter  $\mathbf{F}$  is constructed from a model of the pulse shape and the noise. The noiseless signal  $\mathbf{T}_k$  is obtained by averaging together many records with pulses of a known, identical energy. Depending on whether the filter is build in the time [44] or frequency [146] space, the noise is defined by the noise autocorrelation function or by the power spectral density estimated from the pulse-free records. If the noise is stationary,  $\mathbf{W}\mathbf{T}_k$  is a convolution or a simple product in the time or frequency space, respectively.

This pulse analysis is optimal under the assumption that [46, 167]: (1) the detector response is linear, (2) the pulse shape for a specific energy is known, (3) the noise is stationary and the autocorrelation function is known, (4) the noise is additive and follows a multivariate Gaussian distribution, (5) the pulses have been acquired while the sensor is in its steady-state condition and the energy from earlier X-rays has been fully dissipated.

In the energy range where the detector response is linear, the pulse shape estimated at one energy could be used to construct the optimal filter for all the energies. In practice, this is never the case and an energy scale calibration program is always required to build an optimal filters look-up table to accurately estimate the incoming photon energy.

Several approaches has been proposed to deal with the detector non-linearity, the non-stationary noise and the position dependency. Those include interpolating the filters for an arbitrary energy [131, 167], Taylor expansion of a continuous pulse shape model to leading order in energy [47], position dependent analysis [135], calculating the energy dependence of the response of the detector operated in electrothermal feedback mode [48, 66], multi-pulse fitting [45], and principal component analysis [24, 33, 49].

When constructing the optimal filter, the time average of the optimally filtered pulse, or equivalently, the zero frequency bin of the filter calculated in the frequency space, is generally ignored. The zero frequency bin however, contains crucial information on slow varying fluctuations at the detector and the read-out system level and discarding it might result in a signal-to-noise reduction. As it was shown by Doriese et al. [36], since the size of the zero-frequency bin is determined by the pulse record-length, the energy resolution of a TES depends as well on the record length. An optimal record length does exist, which is typically defined by the detector internal time constants, the count-rate and the computational resources. It is however possible to at least partially recover the energy resolution degradation by correcting the baseline signal after linear fitting the data before and after the pulse. A post-filtering correlation analysis of the filtered pulse-height and the detector baseline level is routinely used as well to mitigate the effect of slow detector drifts occurring during the pulse acquisitions.

The photon flux experienced by a single pixel during bright sources observation could be so high that it becomes impossible to isolate each single photon and perform optimal filtering. Defocusing techniques could be used to spread the high X-ray flux over a large number of pixels in the array. On the ESA's Athena mission for example, a defocusing of 35 mm (with respect to the nominal focal length of 12 m) will enable the observations of extremely bright galactic sources with fluxes up to  $\sim 1$  Crab, with only limited spectral resolution degradation [77, 117].

On a space telescope, most of the data are processed on board. The main on-board processes consist of the trigger algorithm, the event reconstruction algorithm to estimate in real time the arrival time and pulse energy, and the filter generation to compute the template and the optimal filter. The energy scale and the energy scale calibration processes performed on ground shall convert the biased energy estimate into calibrated units, by using fiducial photons from calibration sources. Given the limited amount of computational resources and the limited transmission rate of the satellite telemetry, only a small amount of information is transmitted to Earth. At high photon fluxes, a good strategy is required to estimate the pulse heights with high resolution in the presence of event pile-ups. X-ray instruments on board of the Astro-E [18] and Hit-

omi (Astro-H) [148] introduced the *event grading* approach as illustrated in Fig. (5). The X-IFU instrument

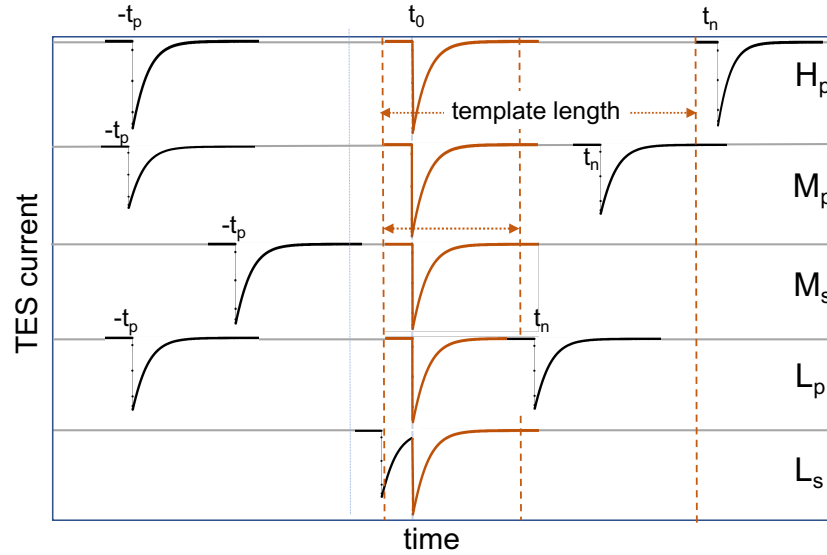


**Fig. 5** Definition of grade for pulse, where  $t_p$  is the time since previous pulse and  $t_n$  is the time until next pulse. The labels  $H_p$ ,  $M_p$ , or  $L_p$  indicate the high-, medium- and low-resolution primary events, respectively. The events following the primary  $M_p$  or  $L_p$  events are labelled as secondary with an  $s$  suffix [149].

shall follow a similar grading definition. The event grading algorithm qualifies the detected pulses according to the proximity of other events in the same record. On X-IFU, High resolution events corresponds to isolated pulses not affected either by preceding or succeeding ones and have a resolution of 2.5 eV at 7 keV. Medium and Low resolution events have a resolution of  $> 2.5$  and  $> 3$  eV, respectively, degraded by another pulse arriving too early after the main one. Fig. (5) shows the definitions of the grades used on Hitomi. A  $p$  suffix denotes that the current event occurred at least  $n$  samples after the previous event. When the interval before the next event is more than  $n$ , between  $m$  and  $n$ , or less than  $m$  samples, the current event is designated  $H_p$ ,  $M_p$ , or  $L_p$  (high/medium/low-resolution), respectively. The events following the primary  $M_p$  or  $L_p$  event are labelled as secondary with an  $s$  suffix [149].

## Detector Design

### TES Properties

The TES is the core of an X-ray microcalorimeter. Various types of superconducting films have been successfully used for different applications: a single layer of tungsten [97, 122], alloys such as Al-Mn [67], and proximity-coupled bilayers (or multilayers) made of Ti/Au [111], Mo/Au [25, 40, 43, 116], Mo/Cu [115], Ir/Au [85], and Al/Ti [2, 98]. These different TES films can all be designed to achieve transition temperatures of 50-100 mK, which is essential for high resolution spectroscopy. The superconducting leads connecting the TES to the rest of the bias circuit must have a higher transition temperature and critical current with respect to the TES film. Niobium is widely used for the leads, but other superconductors such as niobium nitride, molybdenum, and aluminum are also applied.

The TES pixel geometry as well as the design of the coupling between the TES bilayer and the X-ray absorber has direct impact on various properties of the detector. This includes the thermal conductance to the bath [62, 65, 108, 169], the TES transition smoothness and uniformity [133, 173], the susceptibility to the external magnetic field, the detector normal state resistance [57, 109, 126, 169], and the overall detector

noise [34, 106, 124, 154, 159]. In particular, the pixel design optimization is different depending on whether the X-ray microcalorimeters are DC or AC biased [55]. Additional normal metal layers such as 'banks' that run down the edges of the device, parallel to the direction of current flow, and 'zebra-stripes', that run perpendicular to the current flow, were widely explored in early TES design for empirically controlling the transition shape and noise properties [95, 154]. Whereas the use of zebra-stripes has been found to be beneficial to some designs, they can introduce additional inhomogeneity into the film properties (non-uniform current and magnetic field distribution), which greatly complicates the device physics. This can be detrimental to device performance, particularly reproducibility and uniformity in large format arrays [133, 139, 159, 173]. Thus, these types of features are not universally adopted on all TES devices [106, 142]. Understanding all these geometry dependent effects on TES performance has been an a very active area of research and has enabled better control of the device properties and ever improving energy resolution.

### ***Thermal Isolation***

If the thermal conductance ( $G_{bath}$ ) from the sensor to the heat-bath is too great, the pixel response time may be so fast that it becomes impractical to measure the electrical pulses with the available readout bandwidth. For this reason, it is important to limit the thermal coupling to tune the speed of the detector to meet both the count-rate requirements of the application and bandwidth requirements of the readout. The conductance to the heat-bath depends on the material and geometry of the sensor [108, 169] and the substrate on which it is deposited. Thermal control is often achieved by isolating the TES on thin SiN (or SOI) membranes which are typically 100 nm to a few  $\mu\text{m}$ 's thick. In the 2-D ballistic phonon transport limit  $G_{bath}$  will scale with the perimeter of the TES in contact with the membrane and scale as  $\sim T^2$  [65, 144]. Additional thermal control has been demonstrated by engineering slots in to the membrane to reduce the phonon emission and thus the conductance to the bath. Metalization layers can also be added to the surface of the membrane to either enhance [62] or suppress [174] the phonon transport without changing the geometry of the TES itself. TESs can also be directly fabricated on bulk Si substrates. Without the isolating membrane  $G_{bath}$  will be limited by the acoustic mismatch (Kapitza boundary resistance) between the TES and the substrate, and/or electron phonon decoupling [164]. The  $G_{bath}$  from acoustic mismatch will scale as the area of the TES in contact with the substrate and as  $T^3$ . Whereas electron-phonon decoupling scales as the volume of the sensor and  $T^5$  (or  $T^6$ ). Whichever term dominates will depend upon the geometric details of the devices and the temperature of operation.

### ***Absorber Design and Properties***

For X-ray applications where high density, high fill-factor arrays are required, the absorbers are typically cantilevered above the TES and underlying membrane, making thermal contact with the TES via support columns. The absorber needs to rapidly thermalize the photon energy and conduct it to the TES. If the thermal diffusion from the absorber to the sensor is insufficient, the pixel may exhibit excess thermal noise and position dependent resolution broadening (which occurs when the measured signal at the TES depends on the photon absorption position). The absorber material may also contribute significantly to the total heat-capacity, which is an important design parameter used to tune the desired pixel energy range and resolution. Thus, the composition and geometry of the absorber must be optimized to provide the necessary thermal diffusion and heat-capacity, whilst also achieving the desired vertical quantum efficiency (stopping power) for incident X-rays. High-Z metals such as Au are ideal because they have short X-ray attenuation lengths and thermalize quickly. However, the large carrier density means they also have a relatively high specific heat, making them less ideal for applications requiring large area, high stopping power and high energy resolution. The semi-metal Bi is also an interesting candidate material because it has an intrinsically low carrier density and specific heat. However, the thermalization properties of Bi are highly dependent on the deposition method. TESs with evaporated Bi absorbers have shown non-Gaussian broadening in the measured X-ray spectral response (commonly referred to as 'low energy tails'). This is

not fully understood, but may be related to the trapping of energy in long lived states. Electroplated films tend to have larger grains than than in evaporated films and can achieve a higher Residual-Resistivity Ratio (RRR), defined as the ratio of the resistivity of a material at room temperature and at 4 K, and better thermal characteristics [20, 170]. Electroplated absorbers have shown the ability to achieve high resolution spectra without significant spectral broadening features [6, 20]. For applications where large area absorbers are required, composite Bi/Au absorbers can be used to combine the best properties of both materials. This is the approach for the Athena/X-IFU detectors where a bottom 1  $\mu\text{m}$  Au layer provides the desired heat-capacity and rapid thermal diffusion to the sensor. A 5  $\mu\text{m}$  Bi layer is added on top, which provides additional stopping power without adding significant additional heat-capacity. These designs provide  $> 90\%$  vertical quantum efficiency at 7 keV combined with  $> 96\%$  filling-factor. To minimize the effect of the absorption of the stray light in the detector, it is also desirable to increase the reflectivity of the absorber for long-wavelength infrared radiation. For this purpose, a Au capping layer on top of the Bi can be added. For pixels being developed for the Athena/X-IFU instrument, an increase in reflectivity, from 45% to 80%, has been measured at room temperature after adding a 40 nm Au capping layer [68].

### Current State of the Art

TES detectors for X-ray astrophysics applications have now achieved exquisite resolution performance over a broad range of energies. At an energy of 5.9 keV (Mn-K $\alpha$ ) TES microcalorimeters can routinely achieve below 2 eV. DC-biased devices developed for various mission concepts at NASA/GSFC, using Mo/Au bilayers and either Au or Au/Bi absorbers, have demonstrated around 1.6 eV FWHM at 5.9 keV (Mn-K $\alpha$ ) [24, 106, 138]. With the best energy resolution performance to date being 1.3 eV FWHM [127]. This was achieved on a 12  $\mu\text{m}$  TES with  $31 \times 31 \mu\text{m}^2$ , 4  $\mu\text{m}$  thick Au absorber. This very small pixel design is being developed of high angular resolution applications such as NASA's Lynx [7]. At an energy of 1.5 keV (Al-K $\alpha$ ), sub-eV resolution has now been achieved several times with a best resolution of 0.7 eV FWHM [88] (see Fig. (6)).

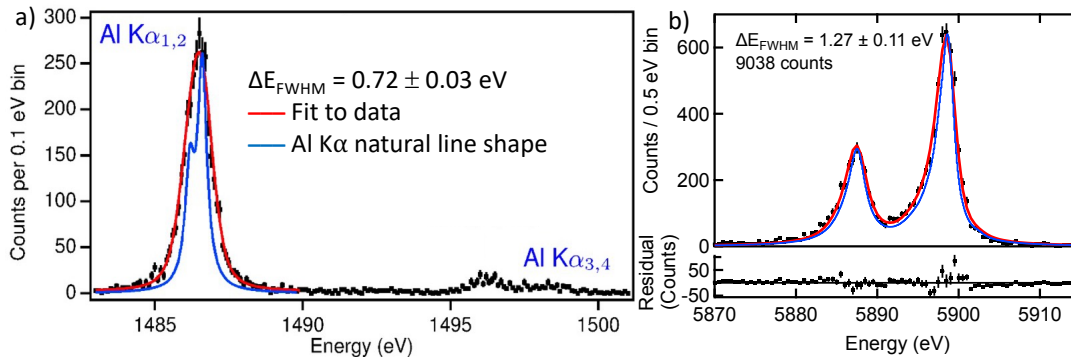


**Fig. 6** Best achieved spectral resolution in TES microcalorimeters at an energy of a) 1.5 keV (Al-K $\alpha$ ) [88] and b) 5.9 keV (Mn-K $\alpha$ ) [127]. The blue lines are the natural line shapes of the line complexes and red lines are the fit to data. These are both DC-biased Mo/Au bilayer TESs developed at NASA/GSFC.

Similar performance has been achieved recently under AC bias using pixels made of Ti/Au TESs with a  $250 \times 250 \mu\text{m}^2$ , 2.35  $\mu\text{m}$  thick Au absorber, developed at SRON and optimized for the FDM readout of Athena/X-IFU-like instruments on future X-ray missions. In Fig. (7), the Mn-K $\alpha$  spectra for two pixels, biased respectively at 1.2 and 4.0 MHz, are shown. The detectors have a  $T_c \simeq 80\text{mK}$ , heat capacity  $C = 0.76\text{pJ/K}$ , normal resistance  $R_N \simeq 200\text{m}\Omega$  and a thermal conductance to the bath  $G_{bath} \simeq 50\text{pW/K}$ .

These results are representative of the best single pixel spectra achieved to date in X-ray microcalorimeters. The expected performance of a large format array in a space flight instrument will, however, typically

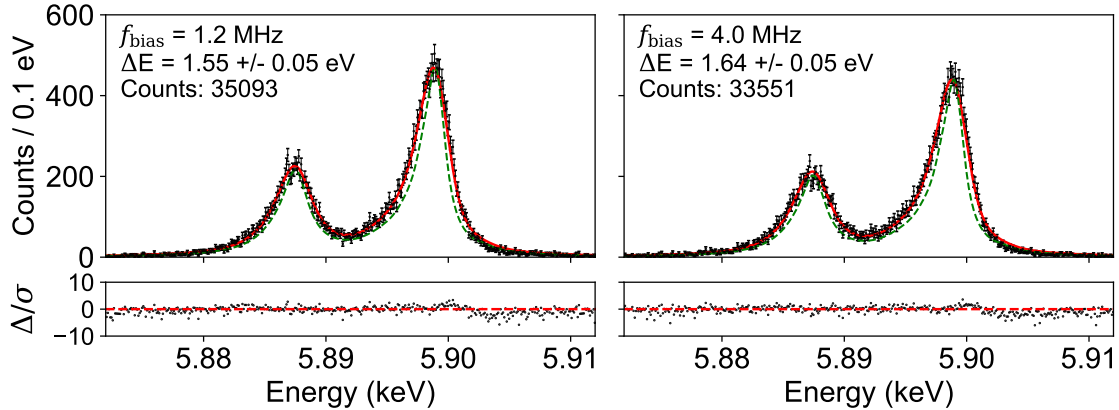


**Fig. 7** Best achieved spectral resolution at 5.9 keV (Mn- $K\alpha$ ) with Athena/X-IFU-like TiAu TES microcalorimeters developed at SRON and AC biased respectively at (left figure) 1.2 and (right figure) 4.0 MHz. The green-dashed line is the natural line shape of the Mn- $K\alpha$  complex.

be somewhat worse than the best individual pixel results measured in a laboratory environment. This is due to a variety of additional sources of noise associated with a large instrument and its environmental conditions. This includes thermal cross-talk between pixels in the array, electrical cross-talk in the bias and readout circuitry, noise from the multiplexed readout electronics, drifts from the instrument environment, noise from particle background events, and noise from micro-vibrations. This means that the individual pixel resolution must be optimized to be lower than the final instrument requirement. For the Athena/X-IFU satellite instrument [11], for example, the individual pixel resolution must be less than 2.1 eV at 7 keV in order to satisfy the full instrument requirement of 2.5 eV.

## Physics of the Superconducting Transition

### *The Superconducting Transition*

The superconducting transition of a TES, since its invention, has been described, according to the well established microscopic (BCS theory [9]) and macroscopic theory of superconductivity in low critical temperature  $T_{ci}$  material. In particular, the macroscopic Ginzburg-Landau theory [87] turned out to be rather successful in explaining the physics near the superconducting transition.

However, while the physics of conventional superconductors is well understood, in two dimensional superconducting films driven in the transition by a large current, like TESs, the observed phenomena are more difficult to explain. For many years, the interpretation of the observed properties of the TES superconducting transition, such as  $T_c$ , width  $dT_c$ , and steepness  $dR/dT$ , was given in the framework of large transport current, Joule heating, self-magnetic field, film impurities, phase slips effects, and vortices generations and annihilations [70]. Interesting enough, researchers overlooked for many years the potential impact on the transition shape of the higher  $T_c$  superconducting leads connecting to the TES bilayer. Superconducting structures, in the form of sandwiches or bridges, consisting of a combination of superconducting and normal metal films or superconducting films with different  $T_c$  has been studied since the 70's in the framework of superconducting junctions and weak links [92]. It was first reported by Sadleir et al. [123, 124] that TES structures behave as a superconducting weak-link due to the long-range longitudinal proximity effect originating from the superconducting Nb leads. Their conclusion was based on three solid experimental findings: (i) the exponential dependence of the critical current  $I_c$  upon the TES length  $L$  and the square root of the temperature difference  $T - T_{ci}$ , with  $T_{ci}$  the intrinsic critical temperature of the bilayer, (ii) the scaling of the effective transition temperature  $T_c$  and the transition width  $\Delta T_c$  as  $1/L^2$ , and (iii) the Fraunhofer-like



oscillations of the critical current as a function of the applied perpendicular magnetic field. We will discuss the details of these findings in the next section.

The physics of superconducting junctions and weak-links has been extensively treated in many books and publications [10, 92]. In 1962, Brian D. Josephson predicted the existence of several new phenomena in two superconductors weakly coupled to each other by a sufficiently thin insulating material [76]. Josephson argued that a supercurrent should leak through the thin barrier depending on the voltage across the junction following the law of quantum mechanics. Josephson's prediction was experimentally verified few years later by P.W. Anderson and J.M Rowell [4]. These works should be considered as milestones for the starting of a new era for the superconducting electronics and quantum physics. Josephson's predictions turned out to be valid not only in superconducting structures, but in other macroscopic systems as well. The Josephson effects have been observed for example in the beautiful experiments with superfluid He [32] and Bose-Einstein condensates in trapped-atom interferometers [91].

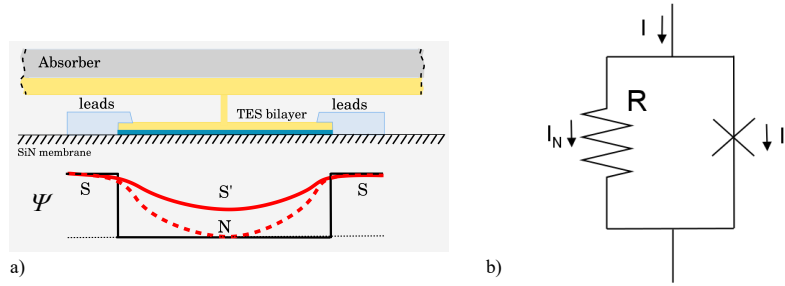


**Fig. 8** a) Schematic representation of a TES-lead system as a superconducting weak-link. The dashed area is the silicon nitrite membrane, the bluish layer is the TES superconducting film (Ti,Mo,..), the yellow layer is the Au film of the TES-absorber system and the grey area represents the Bi layer on top of the absorber. As shown below the drawing, in the proximity of the leads, the spatially varying superconducting order parameters  $\Psi$  of the TES bilayer is enhanced. b) The RSJ model.

The phenomena described by Josephson are summarized in two fundamental equations, which describe respectively a DC and an AC effect:

$$I_J(\varphi) = I_c \sin \varphi \quad (11)$$

and

$$V(t) = \frac{\hbar}{2e} \frac{\partial \varphi}{\partial t}. \quad (12)$$

According to the first equation (dc Josephson effect) the superconducting current has a sinusoidal dependence to the phase difference of the weak-link, i.e. the current through the weak-link is zero when the phase difference is zero, or a multiple of  $\pi$ , and  $I(\varphi)$  is a periodic function with period  $2\pi$ , such that a change of the current flow direction will cause a change of sign in  $\varphi$ . The second equation (ac Josephson effect) states that the rate at which the phase difference  $\varphi$  changes in time is proportional to the voltage across the weak-link. Both Eqs. (11) and (12) can be derived using a straightforward quantum-mechanics formalism describing a two-energy-level system, as it was done for example by Feynman in one of his lectures [41]. When the junction is a narrow bridge or a thin normal metal film, the dc Josephson equation (Eq. (11)) can be derived following a different approach as described by Aslamazov and Larkin [5]. They showed that, for weak-links with length  $L$  smaller than the superconductors coherence length  $\xi$  ( $L \ll \xi$ ), the supercurrent density through the weak-link can be derived from the two Ginzburg-Landau equations as a result of interference of the wavefunctions of the two coupled superconductors.

If the current applied to the junction (or weak-link) exceeds the critical value  $I_c$ , dissipation occurs and a normal electron or quasiparticle current  $I_N$  starts flowing through the junction as well, in parallel with the superconducting Josephson current  $I_J$ . The total current  $I$  in a junction, with normal-state resistance  $R$ , is then the sum of the normal current  $V/R$  and the Josephson current  $I_J = I_c \sin \varphi$ :

$$I = I_c \sin \varphi + \frac{\hbar}{2eR} \frac{\partial \varphi}{\partial t}. \quad (13)$$

Eq. (13) is the basic equation of the so-called resistively shunted junction model (RSJ), which describes the system as an electrical circuit consisting of a Josephson junction in parallel with a normal resistance (Fig. (8).b).

A typical TES, fabricated from a bilayer with intrinsic critical temperature,  $T_{ci}$ , smaller than the critical temperature of the leads  $T_{cL}$ , can be treated as a superconducting  $SNS$  or  $SS'S$  weak-link [54, 92], with the bilayer being  $N$  when  $T > T_{ci}$  and  $S'$  when  $T < T_{ci}$ .

In some devices however, the Josephson effects described above become less evident and tend to disappear. The TES operates in a stronger superconducting regime, depending on the exact shape of the  $I_c(T)$ , the bias current and the operating temperature. As the temperature is further reduced to  $T \ll T_{ci}$ , the measured critical current follows the behavior typical of the Meissner state for a strongly coupled superconductor. Before the discovery of weak-link effects in TES's, Irwin et al. [72] proposed a simple two-fluid model to describe the total current through a TES biased in the resistive transition

$$I_{TES}(T) = c_I I_c(T) + \frac{V_{TES}}{c_R R_N} \quad (14)$$

This model is a simplified form of the Skocpol-Beasley-Tinkham (SBT) model [7] of a resistive transition for a superconductor with phase slip lines (PSL) assuming a constant ratio of the time-averaged critical current to the critical current. The model defines a supercurrent as some fraction ( $c_I$ ) of the critical current, and a quasiparticle current, which is equal to  $V_{TES}$  divided by some fraction ( $c_R$ ) of the normal resistance. Although it does not provide a physical mechanism for the onset of resistance, the two fluid model has been further used by Bennet et al. [13, 108, 155] to make qualitatively good prediction of the logarithmic derivatives of resistance with temperature and current ( $\alpha$  and  $\beta$ ) of TESs used in X-ray and gamma spectrometers. The original SBT or PSL model, which the two-fluid model is based upon, was later on used by Bennet et al. to explain the bi-stable currents observed in some regions of the IV curve of TESs [15]. Their finding might suggest that, for TESs outside the weak-link regime, phase-slip lines could be the mechanism for the observed resistance.

### ***Josephson Effects in DC and AC Biased TESs***

In the current and the following sections, we elaborate more on the implication of the Josephson effects on the performance of TESs. The stronger evidence of the behaviour of TES structures as superconducting weak-links due to the long-range longitudinal proximity effect (LoPE) originating from the superconducting Nb leads is the peculiar dependence of the critical current on the temperature  $T$ ,  $I_c(T)$ , and on the magnetic field  $B$  applied perpendicular to the direction of the current flow,  $I_c(B)$ . The former shows the exponential dependence upon the TES length  $L$  and the square root of the temperature difference  $T - T_{ci}$ :

$$I_c(T, L) \propto \frac{L}{\xi(T)} e^{-\frac{L}{\xi(T)}}, \quad (15)$$

with  $\xi(T) = \xi_i / (T/T_{ci} - 1)^{1/2}$  for  $T > T_{ci}$ . The latter, for  $T \gg T_c$ , take a form similar to the well known Fraunhofer pattern characteristic of many Josephson structures [10, 92]:

$$I_c(B) = I_{c0} \left| \frac{\sin\left(\pi \frac{B}{B_0}\right)}{\pi \frac{B}{B_0}} \right|, \quad (16)$$

The periodicity of the oscillations is  $B_0 = \Phi_0 / (wL)$ , where  $L$  is the junction length,  $w$  the width and  $\Phi_0 = 2\pi\hbar/2e = 2.07 \times 10^{-15}$  Wb is the flux quantum. The equation above assumes a sinusoidal current-phase

relationship, which corresponds to a uniform current density distribution  $J$  at zero applied field, and the presence of negligible screening currents [10].

The longitudinal proximity effect was observed over extraordinary long ( $L > 100 \mu\text{m}$ ) distances and it is responsible for the enhancement, in the proximity of the leads, of the spatially varying superconducting order parameters  $\Psi$  of the TES bilayer (Fig. (8)a). It has been shown as well [124] that the order parameter is suppressed in proximity to normal metal structures deposited along or on top of the TES due to the lateral inverse proximity effect (LaiPE).

Both the effects described by Eqs. (15) and (16), have been experimentally observed over a broad range of TES sizes and geometries, both under DC and AC biasing [57, 123, 124, 139, 169].

The resistively shunted junction (RSJ) model, introduced above, describes very successfully the macroscopic behaviour of superconducting weak-links of many different kind. The RSJ model was first formalized for a dc-biased TES in the work of Kozorezov et al. [83], which shows how to derive the TES resistive transition analytically following the Smoluchowski equation approach for quantum Brownian motion in a tilted periodic potential in the presence of thermal fluctuations [26]. The same approach can be used to calculate exactly the intrinsic TES reactance, which has important implications on the TES response, in particular when operating under MHz voltage biasing [56].

The plot in Fig. (9) gives an example of a TES resistive transition surface  $R(T, I)$  calculated following the approach described above.

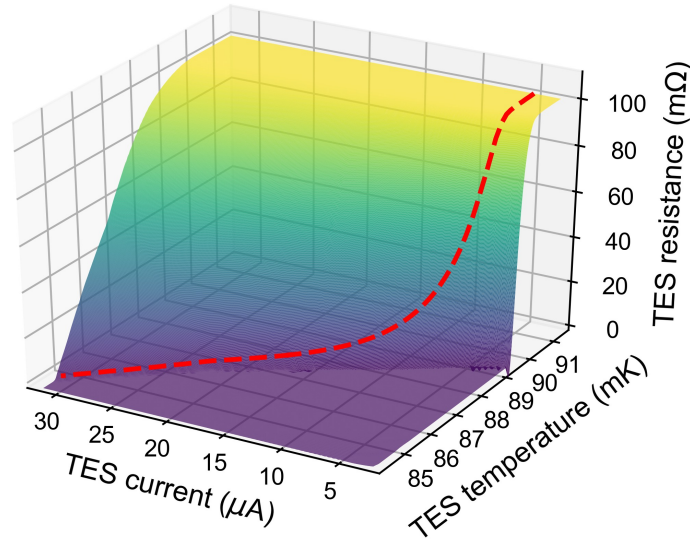


**Fig. 9** Calculated resistive transition curve  $R(T, I)$  for a TES microcalorimeter as described by Kozorezov et al. [83]. The dashed red line is the equilibrium curve across the transition following the detector power law.

From the Josephson derivation in Eq. (13), the total current in the TES  $I(t)$  is the sum of two components, the Josephson current  $I_J(t)$  and a quasi-particle (normal) current  $I_N = V(t)/R_N$ . In the most comprehensive case, the potential across the TES is the sum of a DC and AC voltage  $V_{TES}(t) = V_{dc} + V_{pk} \cos \omega_0 t$ . When the TES is dc biased,  $V_{dc}$  is the constant voltage applied to the TES and the second term accounts for any potential ac excitation of peak amplitude  $V_{pk}$  injected into the bias circuit. In the ac bias case,  $V_{dc} = 0$ , and  $V_{ac} = V_{pk} \cos \omega_0 t$  is the applied voltage bias with amplitude  $V_{ac} = V_{pk}$  and frequency  $\omega_0 = 2\pi f_{bias} = \omega_{bias}$ , that drives the TES into transition. The ac voltage across the TES forces the gauge invariant superconducting phase  $\varphi$  to oscillate at  $\omega_0$ ,  $\pi/2$  out-of-phase with respect to the voltage. The  $\varphi$  peak value depends on  $V_{pk}/\omega_0$ . From Eq. (12), the gauge invariant superconducting phase can be written as  $\varphi(t) = 2e/\hbar \int V_{TES}(t) dt$  and the Josephson current density becomes [10]

$$J_J(t) = J_c(T) \sin \left[ \frac{2eV_{dc}}{\hbar} t + \frac{2eV_{pk}}{\hbar\omega_0} \sin \omega_0 t + 2\pi \frac{A_{eff}(B_{\perp,DC} + B_{\perp,AC}(t))}{\Phi_0} \right]. \quad (17)$$

where  $A_{eff}$  is the effective weak-link area crossed by the dc ( $B_{\perp,DC}$ ) and ac ( $B_{\perp,AC}$ ) perpendicular magnetic field, respectively. The  $B_{\perp}$  field is generally a combination of an external field and the self-magnetic field generated by the current flowing in the TES and the TES leads [139]. The equation above is the generalized equation for the Josephson current density in a weak-link and shows the dependency of the current density on the DC and AC voltage across the weak-link and the magnetic field applied perpendicular to the current flow. In the stationary case,  $\frac{d\varphi}{dt} = 0$ , and in the presence of a perpendicular constant magnetic field and uniform current distribution, Eq. (17) reduces to Eq. (16), after the integration over the weak-link area  $A_{eff} = wL$  [10].

At zero magnetic field and under strict DC biasing ( $V_{dc} \neq 0, V_{ac} = 0$ ), the phase  $\varphi$  varies in time and an alternating current is generated,  $J(t) = J_c(T) \sin \left[ \frac{2eV_{dc}}{\hbar} t \right]$ , with  $\omega_J = 2eV_{dc}/\hbar = 2\pi \times 483.6 \text{ [MHz]} V_{dc}/[\mu\text{V}]$  equal to the Josephson oscillation frequency. In TES micro-calorimeters, the typical dc bias voltage,  $V_{dc}$ , is of the order of 40 to 80 nV, depending on the TES geometry and resistance. For these voltages, the Josephson oscillations occur at frequencies between 20 to 40 MHz, which are generally well outside the read-out bandwidth. We will see in the next section, however, that that mixed-down effects might occur, in particular in the noise, observable in the detector kHz bandwidth.

In the frequency division read-out scheme, the TES detectors are AC biased and  $V_{dc} = 0$  in Eq. (17). It can be shown [55, 56], that an alternating current is then generated through the TES  $\pi/2$ -out-of-phase with respect to the applied voltage  $V_{ac}$ . This is equivalent as saying that a TES possesses an intrinsic reactance, which becomes non-negligible when exciting the device at the MHz frequencies [56, 83].

In Fig. (10).a, the TES in-phase current  $I_I$  and the quadrature current  $I_Q$  normalized to  $I_I$  are shown as a function of the TES voltage for an AC-biased low resistance  $50 \times 50 \mu\text{m}^2$  MoAu TES X-ray calorimeter fabricated at NASA/GSFC [106]. The quadrature component of the current is a direct measurement of the Josephson current described by Eq. (17). The steps observed in the in-phase current are the results of the intrinsic non-linear reactance expected when a TES behaves as weak-link [58].

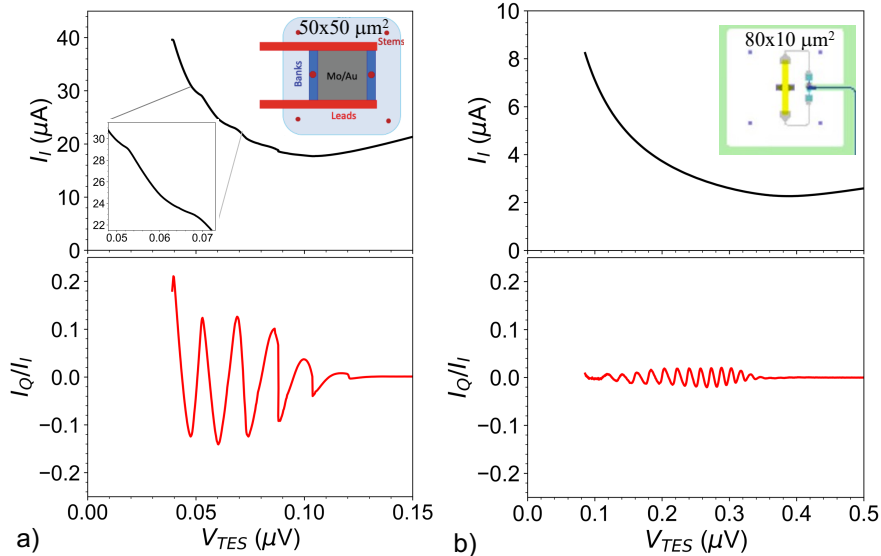


**Fig. 10** a) Current-to-voltage characteristic of a Mo/Au  $50 \times 50 \mu\text{m}^2$  ( $AR = 1:1, R_N = 8\text{m}\Omega$ ) TES X-ray calorimeter fabricated at NASA/GSFC. The pixel is AC biased at 4.0 MHz. The TES in-phase current,  $I_I$ , and the quadrature current,  $I_Q$  (Josephson current), normalized to  $I_I$  are shown. b) Mitigation of the weak-link effects for the AC bias read-out by employing the high normal resistance, high-aspect ratio devices developed at SRON. The graphs shows  $I_I$  and  $I_Q/I_I$  for a Ti/Au  $80 \times 10 \mu\text{m}^2$  ( $AR = 8:1, R_N \simeq 200\text{m}\Omega$ ) TES X-ray calorimeter, AC biased at 4.0 MHz.

As predicted by the theoretical model presented in this session, the observed non-ideal behaviour of AC biased devices, caused by the Josephson effects, can be minimized by increasing the TES normal resistances,  $R_N$ , and by designing the TESs with higher aspect ratio (AR) [58, 169]. In TESs with higher  $R_N$ , operating at the same power  $P_J$ , the gauge invariant phase difference across the Josephson weak link is maximized since  $\varphi \propto \sqrt{P_J R} / f_{bias}$  and the TES is less affected by the Josephson effects. In Fig. (10).b, we give an example of the mitigation of the Josephson effects achievable by using high aspect ratio TESs. We show the current-to-voltage characteristics of an SRON Ti/Au  $80 \times 10 \mu\text{m}^2$  (AR = 8:1,  $R_N \simeq 200 \text{m}\Omega$ ), measured under AC bias. The device has a  $P_J \sim 1\text{--}2 \text{pW}$ , compatible with the X-IFU requirement and is biased at  $f_{bias} = 4.0 \text{MHz}$ . The amplitude of the Josephson current is drastically reduced in the long, high resistance devices, in contrast to the detector of Fig. (10).a. These novel TES design leads to a smoother resistive transition, even at high bias frequency.

The strong non-linear nature of the Josephson current described in Eq. (17) could challenge the calibration of the detector response as a function of energy both under AC and DC bias. In the former case, non-linearity arises from the bias-dependent detector reactance, in the latter case from the strong dependency on the external magnetic field. The Josephson effects have to be minimized, for both the read-out schemes, by a proper detector design. The optimization process is complex and still a subject of active research [35, 140, 156]. As it is illustrated in Fig. (11)a, the high aspect ratio design drastically reduces

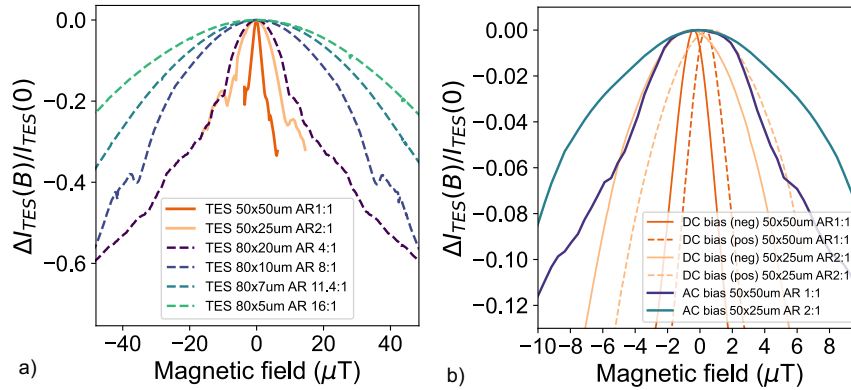


**Fig. 11** a) Relative change in the TES current as a function of the magnetic field perpendicular to the current flow for several SRON-fabricated Ti/Au TESs with low and high aspect-ratio geometry. The detectors are biased at their optimal value respectively under AC (bluish dashed lines) and DC voltage (orange lines). b) Magnetic field effect in pixels with low aspect ratio geometry operated respectively under AC (blue lines) and DC bias (orange lines). The solid and dashed lines of the DC bias case indicate respectively the negative and positive biasing.

the dependency on the perpendicular magnetic field. The relative change in the TES current at the nominal bias condition is shown as a function of the magnetic field perpendicular to the current flow for SRON-fabricated devices with different aspect ratio. The low aspect ratio geometry (orange lines) are typically used in the DC bias read-out due to their low normal resistance [143], while the large normal resistance and high aspect ratio geometry (bluish dashed lines), envisioned to minimize the detector reactance, have been used for the AC bias read-out [3].

The alternating current in the AC bias configuration mitigates the effect of the self-magnetic field observed in DC bias devices thoroughly discussed by Smith et al. [139]. The effect is shown in Fig. (11).b where identical pixels with low aspect ratio design have been measured both under AC and DC bias.

### ***Implication of the Weak-Link Behaviour on the Detector Noise***

The observed excess Johnson noise in TES-based detectors could have a natural explanation within the RSJ theory. Following the work of Likharev and Semenov [93] and Vystavkin *et al.* [158], Kozorezov *et al.* [84] calculated the power spectral density of the voltage fluctuations,  $S_V(\omega)$ , across the TES (considered as a resistively shunted junction), averaged over the period of the Josephson oscillations. They obtained

$$S_V(\omega) = \frac{4k_B T}{R_N} \sum_m |Z_{0m}|^2, \quad (18)$$

where  $Z_{mn}(\omega)$  are the components of the impedance matrix of the biased TES with the index  $m$  standing for the  $m_{th}$  harmonic of the Josephson oscillation at  $\omega_J$ . This approach was used in Koch *et al.* [81] to develop the quantum-noise theory of a resistively shunted Josephson junction and SQUID amplifiers. They showed that to calculate the total low frequency voltage fluctuations, one needs to take into account the mixing down of high frequency noise at harmonics of the Josephson frequency. Following these reasoning, in [84], the authors argued that the only source of the intrinsic electrical noise in the TES is the *equilibrium* Johnson normal current noise [93] enhanced by the nonlinear response of the weak link. Within this framework, there is no need to introduce the nonequilibrium Markovian fluctuation–dissipation relations as discussed in [69]. The RSJ model predicts a significantly higher broadband noise, with respect to the non-equilibrium Johnson noise theory proposed by Irwin, at the lower part of the resistive transition, as generally observed in many experiments.

A simpler expression for Eq. (18), based on the approximations explained in [84], has been recently derived by Wessel *et al.* [165, 166] in the form:

$$S_V(\omega) = 4k_B T R \zeta_{RSJ}(I) \quad (19)$$

with  $\zeta_{RSJ}(I) = 1 + \frac{5}{2}\beta + \frac{3}{2}\beta^2,$

where  $R_N$  in Eq. (18) is replaced by  $R$ , given the fact that the thermal fluctuations are associated with the real part of the TES impedance at the equilibrium value. In the same paper, the authors compare the measured Johnson noise for a few TES microcalorimeters [159] with Eq. (19), the general form derived by Kogan and Nagaev [82] (KN) and the prediction from the two-fluid model [14, 165]. In the simplified form of the two-fluid model, no mixed-down noise from high to low frequency is predicted, and the expected noise is typically underestimated. A better agreement with the data is observed with the RSJ and the Kogan–Nagaev models.

In a recent study [61] on the noise of high-aspect ratio TESs under development at SRON for the MHz bias read-out, a very good agreement between the observed Johnson noise and the prediction from the RSJ and Kogan–Nagaev has been demonstrated over a large number of TES designs and bias conditions. The authors concluded that the fluctuation-dissipation theorem generalized for a nonlinear system in thermal equilibrium explains well the observed noise and that it is not necessary to introduce the formalism for a nonlinear TES out of equilibrium described in [69]. By assuming Eq. (19) as the correct expression for the Johnson noise in a TES, de Wit *et al.* [34] performed a study on the impact of the internal thermal fluctuations driven by the TES-absorber coupling design. The work revealed subtle thermal effects and stressed the importance of a proper model for the TES Johnson noise.

### **Detector Calibration Considerations**

The measured spectrum from an X-ray observatory will be a convolution of the astrophysical source with the response function of the instrument. In order to realize the exquisite spectroscopic capabilities of TES detectors on a real flight instrument, this response function must be properly calibrated and variations in the time due to changes in the instrument environment must be accounted for. Uncertainties in the knowledge of the overall system performance can lead to systematic errors in the data, and potentially compromise

science objectives. Extensive calibration procedures, developed for Si thermistor microcalorimeters for the Astro-E and Astro-H missions [38], can be applied to TES technology for missions such as Athena [28, 29].

## Response Function

The response function includes the effective area and line spread function (energy resolution and redistribution) as a function of energy. The effective area describes the X-ray collecting efficiency of telescope and includes contributions from the mirror, optical blocking filters and the detector. At the detector level the array quantum efficiency, including both the vertical stopping power of the absorbers and the geometric filling factor, must be precisely calibrated (at the few % level) as function of energy. This can be achieved through a combination of microscope inspection of the absorber size and gaps between pixels at various point across an array, measuring the change in mass of the detector wafer after the absorber deposition, and directly measuring the transmission of absorber parts at a synchrotron source.

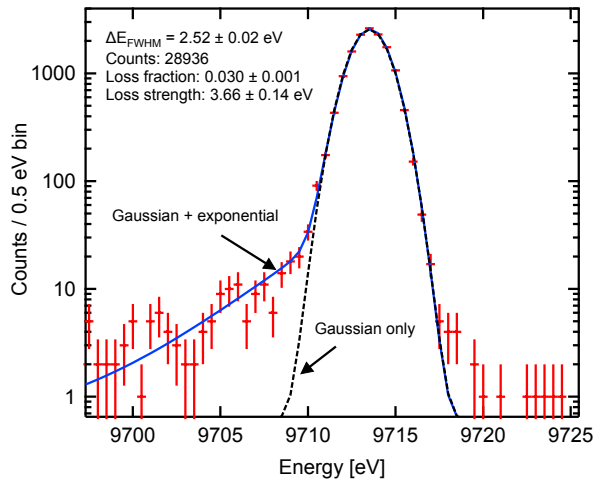


**Fig. 12** Example low energy tail below the main Gaussian core-LSF for 8 pixels in a prototype X-IFU array. The low energy tail accounts for 3% of events and has an exponential folding factor of 3.7 eV. These data was acquired using a channel cut crystal monochromator (CCCM) Au-L source [89] with intrinsic Gaussian line width of  $< 0.5$  eV.

The line spread function (LSF) describes the probability that an incident X-ray event of energy  $E$ , will be measured in a given energy channel  $E'$ . The LSF consists of the Gaussian core and non-Gaussian or extended components. The core-LSF width is dominated by the intrinsic detector and system noise properties and is typically what is used to describe the energy resolution of the detector. Outside of the core, a small fraction of incident events appear re-distributed to lower energies due to various effects related to absorption physics. The re-distributed features or extended-LSF includes near core exponential tails in the spectrum just below the primary line, as well as electron-loss continuum and absorber escape peaks. Understanding and calibrating the LSF is important to be able to correctly interpret the measured spectrum from astrophysical objects. Uncertainties in the energy resolution will particularly affect measurements of the line broadening in astrophysical sources. Even with high purity electroplated Bi and Au absorbers, low level tails in the measured spectrum can typically be observed when using very narrow beam X-ray sources such as a channel cut crystal monochromator (CCCM) [89] or an Electron Beam Ion Trap (EBIT) [114]. An example spectrum is shown in Fig. 12 for a prototype Athena X-IFU detector which shows the Gaussian core and a residual low energy tail. Eckart et al. [39] studied the energy dependence of these residual low energy tails in similar detectors with Bi/Au absorbers and showed that the number of events redistributed to the low energy tail increased with decreasing photon energy.

The electron loss continuum occurs due to partial thermalization of events that are absorbed near the surface of the absorber. The initial photo-electron that is created by the primary X-ray may be scattered out of the absorber. Consequently only a small fraction of the incident X-ray energy is measured by the detector.

This is empirically found to have approximately constant flux per energy interval below the primary X-ray line energy. Only a few % of the total events are redistributed to the electron-loss continuum.

When an X-ray event ejects an inner shell electron, the resulting vacancy may be filled by an outer shell electron and a fluorescent X-ray emitted. If this X-ray escapes the absorber, the detected energy is then equal to the primary X-ray energy less the fluorescent energy of the emitted X-ray. The resulting spectrum will contain a series of 'escape peaks' whose energies depend upon the primary X-ray energy and the absorber composition. In addition to these extended-LSF components, background peaks may be seen due to fluorescent X-ray emission from parts of the experimental apparatus exposed to the source flux. This could include the detector wafer, parts of the detector housing or cryostat and X-ray source itself. Figure 13 shows a measured spectrum from a prototype Athena/X-IFU array [143] including over 200 pixels. These devices have composite Bi/Au absorbers. The spectrum shows the primary Mn-K peaks from the source, as well as the extended-LSF and various fluorescent background peaks. Only the Si-K fluorescence line is fundamental to the detector. The main escape peaks are clearly visible above the electron loss continuum and are from Bi and Au M-shell fluorescent emission.

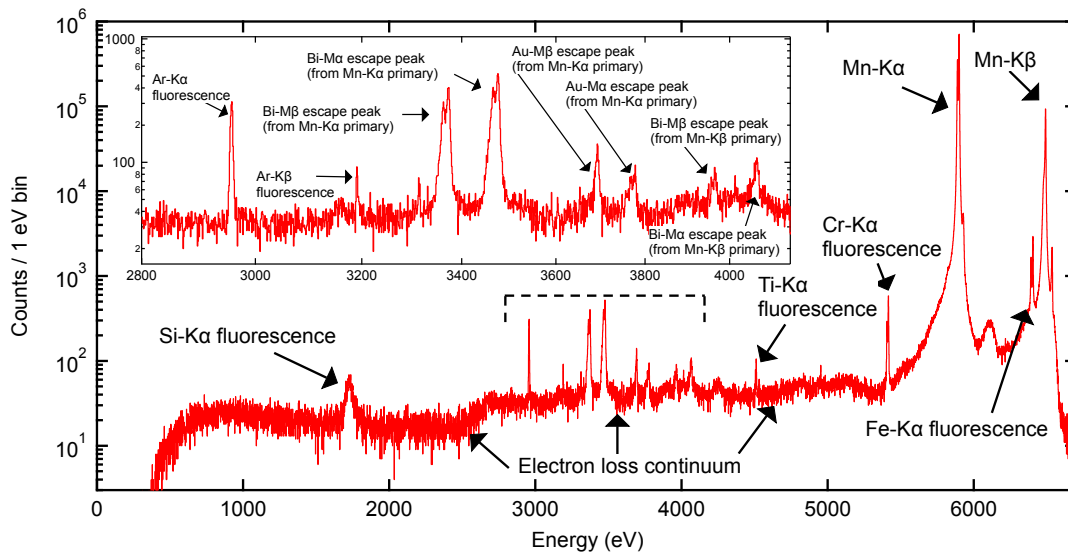


**Fig. 13** Mn-K spectrum from a prototype Athena/X-IFU array including over 200 pixels [143]. The spectrum shows the primary Mn-K $\alpha$  and K $\beta$  lines from the X-ray source, and the background fluorescence and extended LSF features. This includes the electron loss continuum, fluorescence lines from Si (from detector wafer), Ar (from air), Ti, Cr and Fe (from the experimental apparatus), and Bi and Au escape peaks due to M-shell fluorescence. The inset shows a zoom-in of the region from 2.8-4.2 keV (indicated by the dashed line). The abrupt cut-off in the spectrum at 400 eV is due to the event trigger level and is not a property of the detector.

### ***Energy Scale and Sensitivity to Environmental Fluctuations***

The energy scale is a function  $E(PH)$  that relates the output of the event processor,  $PH$  (the optimally filtered pulse height in engineering units), to calibrated energy units,  $E$ . TESs are inherently non-linear detectors and the superconducting-to-normal transition is very difficult to model accurately, thus an empirical approach to gain calibration is required. Fig. (14) shows an example of an energy scale function for a prototype TES detector for X-IFU. The gain function is found by fitting some function (such as a polynomial) to the known positions of the X-ray calibration points as function of optimally filtered pulse height. Gain



errors can arise due to uncertainties in the line shapes and position of the calibration lines themselves as well as due to interpolation errors between the known calibration points.

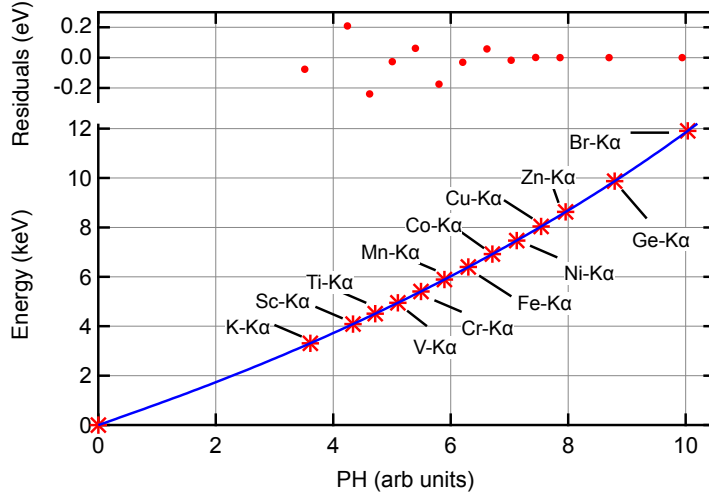


**Fig. 14** Example energy scale function  $E(PH)$  for a prototype Athena/X-IFU pixel measured over the range 3.3 - 12 keV using a rotating target source with 12 different fluorescent targets. Data is fitted with an 8<sup>th</sup> order polynomial. For X-IFU, the energy scale must be known to a level of  $\pm 0.4$  eV for energies up to 7 keV.

Besides determining the gain function at the nominal detector operating points, it is important to understand how the gain evolves with the varying environmental conditions of the instrument. Variations in the detectors environment such as the heat-sink temperature, magnetic field, stray optical/IR power loading and temperature of bias/readout electronics may result in drifts in the detector gain over time. If uncorrected this can result in resolution broadening and error in the absolute energy knowledge. Fluctuations in the TES voltage bias,  $dV_b$ , (due to a thermal drift in the electronics for example), will directly affect the bias point of the TES and therefore affect its gain. Fluctuations in the heat-sink temperature,  $dT_{bath}$  will have a similar impact since it directly changes the operating point of the TES. But it can also slightly affect other properties such as the transition shape (due to the current dependence of the transition). Magnetic field,  $B$ , affects  $R(T, I)$  via the temperature and field dependent critical current  $I_C(T, B)$ . Changes in  $\alpha$  and  $\beta$  directly affect the pulse shape and thus the gain of the detector. The sensitivity of a TES to  $B$  depends on numerous factors including the details of the geometry, whether DC or AC biased, and the magnitude of any self-magnetic field [35, 139, 156]. For a device that shows weak-link behaviour (Fraunhofer-like  $I_C(B)$ ) the pulse-shape may oscillate with  $B$  with the same periodicity seen in the  $I_C(B)$  [133, 140]. The effective area of the TES that threads magnetic flux ( $A_{eff} = \Phi_0/B$ ) determines the periodicity in  $I_C(B)$  and thus  $PH(B)$ . Thus a smaller TES has the potential to achieve less sensitivity to B-field.

One of the most important properties of a TES that affects its gain sensitivity is the electrothermal feedback (ETF). The ETF that arises due to the voltage biased operation of the TES act as a restoring force, countering changes in external environment. Devices with high ETF, often parameterized by the 'loop gain' (see Section ), will generally have more immunity than devices operated in a low ETF regime. For a device with fixed transition properties, the only way to practically maximize the ETF is by ensuring the voltage bias shunt resistor is very much less than the TES operating resistance ( $r_{sh} \ll R_0$ ) and/or the heat sink temperature is much less than the operating temperature of the TES ( $T_{bath} \ll T_0$ ). As an example, Fig. (15) shows the simulated  $dE/dT_{bath}$  as a function of  $r_{sh}/R_0$  and  $T_{bath}/T_0$  for an Athena/X-IFU-like pixel. This illustrates how minimizing these ratios can be effective in reducing the sensitivity to bath temperature drifts. For a flight instrument, minimizing  $r_{sh}$  has to be traded against other practical considerations such as the TES bias source range (lower  $r_{sh}$  requires a larger current source to operate the TES at the same  $R_0$ ), the power dissipation at the 50 mK stage (power dissipated in the shunt resistor scales as  $R_0/r_{sh}$ ), and physical space constraints on the 50 mK stage (smaller  $r_{sh}$  generally requires larger physical area). The lower the  $T_{bath}$ , the shorter the hold-time of the cooling chain adiabatic demagnetization refrigerator (ADR) becomes, unless the cooling capacity of the ADR is increased.

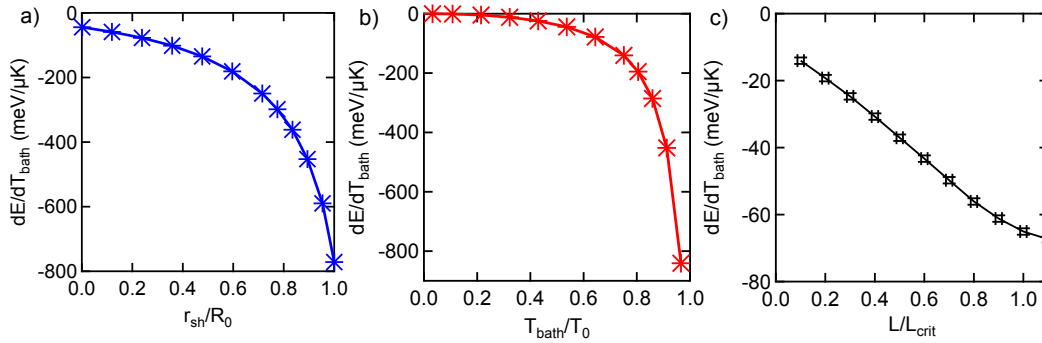


**Fig. 15** Simulated  $dE/dT_{\text{bath}}$  as a function of a)  $r_{\text{sh}}/R_0$ , b)  $T_{\text{bath}}/T_0$  and c)  $L/L_{\text{crit}}$  for an X-IFU pixel at 6 keV. For Athena/X-IFU the baseline design is  $r_{\text{sh}}/R_0 \sim 0.1$  and  $T_{\text{bath}}/T_0 \sim 0.6$  and  $L/L_{\text{crit}} \sim 0.7$ .

From the multiplexed read-out perspective, it is ideal to critically damp the pulses to minimize the requirements on the readout. The effect of adding inductance changes the pulse shape (increases the rise-time, reduces the fall-time and increases the pulse-height). However, this is non-linear with increasing inductance, with larger changes in responsivity occurring (for a given change in  $L$ ) as  $L/L_{\text{crit}}$  approaches unity. Consequently, the pulse shape also becomes more sensitive to changes in its environmental bias conditions. Thus, a side effect of larger inductance is an increased gain sensitivity (Fig. (15) c).

### Drift Correction Algorithms

On the final instrument, any drifts in gain will be monitored using fiducial line(s) generated by a calibration source [157]. The measured drifts can then be corrected during post-processing. The simplest method to correct the gain is to apply a linear stretch factor. This can work well when the detector gain is fairly linear and the scale of the drifts are relatively small ( $\sim$  eV). However in the presence of larger drifts, and particularly for non-linear detectors such as TESs, large residual errors may arise at energies away from the fiducial energy. Porter et al. [121] demonstrated a gain drift correction approach for microcalorimeter detectors (originally developed for the SXS instrument on Astro-H) that takes into account the non-linear shape of the energy gain scale to reduce gain errors over the full bandpass. In this method, reference gain scales are measured (during ground calibration) at three different heat sink temperatures, chosen to envelope the expected variation in operating conditions over the mission lifetime. Drifts are tracked at a single energy using the onboard calibration source and a new interpolated gain scale is derived (as a function of time) using the three reference calibration curves. Although the non-linear correction accounts for the shape of the gain scale, its evolution with variations in the environment may not be uniquely characterized using a single fiducial line. Using simulated TES data, Cucchetti et al. [28] developed a multi-line, non-linear drift correction approach, which used two fiducial calibration lines (Cr- $K\alpha$  and Cu- $K\alpha$  for example) to track the gain instead of one which demonstrated reduced gain residuals across the bandpass. These multi-line approach is being developed for Athena/X-IFU. Cucchetti et al. [27] also investigated a multi-parameter, non-linear drift correction approach that aims to incorporate additional information from the detector baseline-level (the pre-trigger mean of the measured pulse) in the correction algorithm.

### Multi-Pixel TESs

Several practical constraints can limit the number of pixels in the array, both at the focal-plane assembly (FPA) and for the instrument as a whole. These include: the high density of wiring needed to route wires from the interior of the array to the bias circuit and readout components; the physical space required on

the FPA for shunt resistors, Nyquist inductors and readout chips; the associated power dissipation of those additional components; the larger number of readout electronics boxes (which drives instrument mass and power), and the number of interconnects between temperature stages. Position-sensitive microcalorimeters are an alternative approach to arrays of individual TES pixels that enable a larger number of effective pixels in an array, without significantly increasing the complexity of the instrument. This comes with some trade in performance. Position-sensitive microcalorimeters have been proposed in various slightly different forms [73, 110, 134, 137, 145], but the basic principle is to use a single extended absorber, or series of absorbers, connected to one or more TES. Due to the finite thermal conductance between the position of the absorption event and the TES(s), a different characteristic pulse-shape is measured depending upon where the photon has been absorbed. It is this pulse-shape variation that enables position discrimination. This concept is often referred to as 'thermal multiplexing' which, when combined with an electrical multiplexed readout, is a very powerful tool for increasing the effective number of pixels in an array.

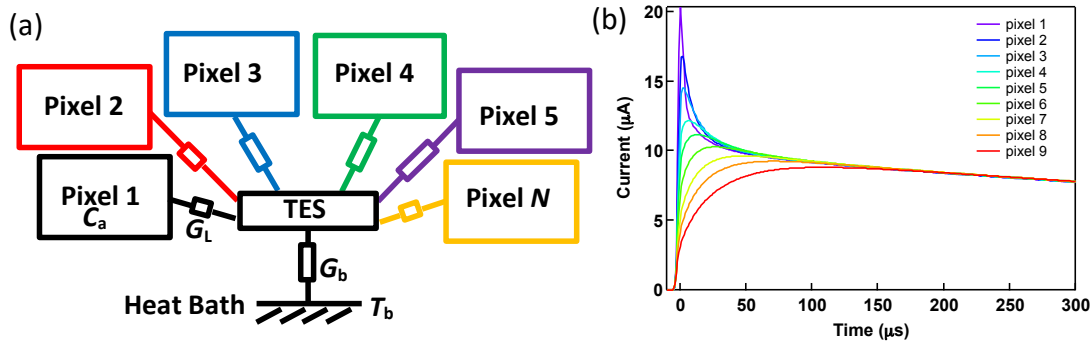


**Fig. 16** a) Thermal design of an N-pixel hydra of the type under development at NASA GSFC. b) Measured average pulses from a 9-pixel hydra [141].

Position-sensitive TESs for X-ray astrophysics were first developed at NASA/GSFC [42, 73]. The currently favoured design is referred to as a 'hydra'. The hydra consists of a single TES connected to series of discrete X-ray absorbers [136]. Figure 16 shows a thermal block diagram of the hydra concept consisting of N X-ray absorbers each with a different thermal 'link' to a TES. This configuration is referred to as a 'star' geometry. The links act as thermal low pass filters. By varying the thermal conductance of these thin metal links (by varying the length and width) the bandwidth of each thermal filter can be tuned to give a characteristic pulse shape for the signals from each of the X-ray absorbers. Decoupling pixels in this way enables position discrimination, but at some expense in energy resolution. The low-pass filtering of the pulse shape attenuates the signal relative to the detector noise and slightly degrades the energy resolution. The more thermally decoupled a pixel, the more degraded  $\Delta E_{FWHM}$  is expected to be from the single-pixel limit. The decoupling of the absorbers also adds a small amount of internal thermal fluctuation noise (ITFN) between the absorber and the TES (as described in Section ). If  $\Delta E_{FWHM}$  becomes too degraded the ability to distinguish pulses will also be compromised. Thus the link conductances must be optimized to maximize the signal-to-noise while maintaining just enough separation between pulse shapes to determine position. The maximum count-rate capability of a hydra is also an important design consideration. The count-rate of a TES is typically limited by pulse pile-up measured in the TES data stream. Thus an N-pixel hydra will have the same maximum count-rate ability as a single pixel TES detector of the same physical size. However, the count-rate per imaging element will be N times lower. The larger the number of pixels in the hydra (the 'hydra factor'), the larger the performance degradation and the more technically complex the design is to implement. Hydrazes can be used for applications where it is desirable to achieve a much larger field-of-view, or improved angular resolution for the same field-of-view, when compared to an array of individual TES pixels (with some trade in performance). See Section for proposed missions that include the use of hydrazes.

Figure 16 also shows the measured average pulse shapes for a 9-pixel star-hydra developed at NASA/GSFC [141]. The largest, fastest rising pulse shape corresponds to the pixel directly coupled to the TES. The pulse

amplitude becomes smaller, and the rise-time slower, as each absorber is further decoupled from the sensor. After the initial, position-dependent equilibration signal, the hydra thermal networks comes in to equilibrium and the pulses from all pixels decay at the same exponential rate (determined by the electrothermal time constant of the hydra). These Mo/Au bilayer TESs had a transition temperature of 46 mK. Each Au X-ray absorber was  $65\ \mu\text{m}$  on the side and  $5.2\ \mu\text{m}$  thick. The achieved resolution was  $\Delta E_{FWHM} = 2.23\ \text{eV}$  at Al-K $\alpha$ ,  $2.44\ \text{eV}$  at Mn-K $\alpha$ , and  $3.39\ \text{eV}$  at Cu-K $\alpha$ . Position discrimination was achieved from the rise-time of the pulses.

To achieve a larger numbers of pixels / TES, it becomes increasingly more challenging to physically layout the internal links, whilst achieving the desired thermal conductances. As a solution, NASA/GSFC proposed a hierarchical 'tree' geometry. In the tree-hydra, instead of connecting every pixel directly to the TES, groups of pixels are connected together by link 'branches', and then 1 pixel from each group connects to the TES via link 'trunks'. The more complex thermal network of the tree-hydras means that more sophisticated position-discrimination algorithms may be required to determine the event position. Prototype tree-hydras have been developed with up to 25 pixels per TES (5 trunks each with 5 branches) for NASA's Lynx mission concept [142]. The authors were able to demonstrate position discrimination using a simple approach to parameterize the rising-edges with two metrics that extracts a fast and slow component to the rise-time. This allowed unique identification of every branch and trunk pixel. These tree-hydras demonstrated  $\Delta E_{FWHM} = 1.66\ \text{eV}$  and  $\Delta E_{FWHM} = 3.24\ \text{eV}$  for hydras with a  $25\ \mu\text{m}$  and  $50\ \mu\text{m}$  absorber pitch, respectively, for Al-K $\alpha$  X-rays [142].

## Applications and Future Technology Needs

### *Ground Based Instrumentation*

X-ray spectroscopy contains diagnostic transitions from ions of every abundant cosmic metal and provides information on plasma temperature, density, elemental and ionic composition. The utility of these diagnostics requires knowledge of large sets of atomic data that describe the physics of the emission process. Ground based, laboratory astrophysics measurements are critical to provide the experimental knowledge needed to bench-mark the atomic models used to interpret high-resolution spectra from celestial observations. There are various facilities worldwide, which can generate laboratory plasmas in controlled conditions: this includes electron beam ion traps (EBIT) and tokamaks (used in fusion energy sciences). By varying the composition and ionization state of a hot gas generated under controlled conditions, one can relate observed X-ray spectra to the conditions of the gas, and then translate that knowledge to real astrophysical observations. The first EBIT to be developed was at Lawrence Livermore National Laboratory (LLNL) in 1985 [90]. EBITs have been extensively used to produce high quality atomic data including accurate wavelengths measurements, line intensity ratios, linear polarizations, and cross-sections to test and benchmark various models theories [21, 50, 113]. Several low temperature detectors systems have been deployed at the LLNL EBIT using silicon thermistor detectors developed from the Astro-E and Astro-H flight programs [119, 120]. A TES based detector system using prototype Athena X-IFU detector and readout technology will be deployed in the near future [143]. A similar TES based spectrometer has been fielded at the NIST Gaithersburg EBIT [147].

In addition to the laboratory astrophysics measurements, X-ray TES microcalorimeters are now commonly employed at a variety of light sources, accelerator facilities, and laboratory-scale experiments carrying out measurements related to synchrotron-based absorption and emission spectroscopy and energy-resolved scattering; accelerator-based spectroscopy of hadronic atoms and particle-induced-emission spectroscopy; laboratory-based time-resolved absorption and emission spectroscopy; X-ray metrology. Further details of these instruments can be found in [37, 155] and will not be discussed further here.

## Next Generation Space Mission Concepts

In this section we briefly describe the TES detector concepts that are under development for the next generation of X-ray observatories as listed in Table 1.

**Table 1** Overview of the characteristic of the TES-based instruments planned for the future X-ray space observatories. Athena is currently in the ESA Phase-A study. The other missions are still in the selection or proposal phase.

Mission	F.o.V. (arc min)	Angular Resolution (arc sec)	Number of Pixels	Energy (keV)	dE (eV)	Eff. Area @ 1 keV (m <sup>2</sup> )
Athena	5	5	~2,400	0.2–12	2–2.5	1.4
LEM	30	15	~16,000	0.2–2	1–2	~0.26
Lynx	1–5	0.5–1	~100,000	0.2–7	0.3–3	0.2–2
Super DIOS	>30	0–15	~30,000	0.2–2	< 2	>0.1
CWE	60	5	~1 M	0.1–3	0.3	10

Mature cryogenic X-ray microcalorimeter instruments using Si thermistor detectors have flown the XQC sounding rocket experiment and in orbit through the Japanese mission HITOMI, and will fly again in 2023 on XRISM. However, the higher performance/lower maturity TES based instruments are unlikely to be realized on a satellite mission until the 2030's. TES detectors have however been flown on the sub-orbital sounding rocket experiment Micro-X (Northwestern University, USA) in 2018 [1]. Micro-X uses TES devices developed at NASA/GSFC with intrinsic energy resolution of 4.5 eV over the energy range of interest (0.1– 2.5 keV). The array consists of 128 pixels on a 600  $\mu\text{m}$  pitch. The launch was intended to observe the supernova remnant Cassiopeia A. A failure in the attitude control system prevented the rocket from pointing and led to no time on target. However in-flight calibration data still provided important information about the performance of these detectors in a flight environment. The mission has recently (August 2022) had a successful re-flight, observing Cassiopeia A, with results and analysis pending.

The Advanced Telescope for High-Energy Astrophysics (Athena) was selected as an L-class mission in ESA's 2015–2025 Cosmic Vision plan and has an anticipated launch date in the late 2030's. Athena was chosen to address the science theme: 'The Hot and Energetic Universe', and as such will answer important questions related to the growth of black holes and large scale structure in the Universe. Athena is the most mature mission concept currently under development. As currently envisioned, Athena will have two main instruments, a wide-field imager (WFI) and an X-ray Integral Field Unit (X-IFU). The X-IFU [11] will comprise of a 2.4k TES pixel array (provided by NASA/GSFC) and will be read out with TDM (NIST/Boulder). The X-IFU will have a field-of-view of 5 arc-minutes and will provide imaging-spectroscopy over the energy range 0.2–12 keV, with an energy resolution of 2.5 eV at energies up to 7 keV. Fig. (17) shows a prototype full scale X-IFU array with 3k pixels in a hexagonal configuration. The TESs are Mo/Au bilayers with a transition temperature of  $\sim 90$  mK fabricated on a 317  $\mu\text{m}$  pitch. The X-ray stopping power is provided by Bi/Au absorbers  $\sim 6$   $\mu\text{m}$  thick. Also shown in Fig. (17) is an energy histogram showing the combined spectral performance at an energy of 7 keV and includes over 200 pixels from a prototype 1k array that was read out using TDM [143].

There are many design issues to consider when developing a complex instrument like X-IFU within the engineering limitations of a satellite. The packaging of the main sensor array chip, the cold read-out electronics stages, the long harness and the warm electronics for a space-born instrument [52, 74, 163] have several challenges related to the interaction between the different components and the thermal, mechanical, and electromagnetic environment. The focal plane assembly (FPA) has to be made robust against cosmic ray radiation [68, 100, 107, 118], infra-red and optical loading [8], thermal fluctuation, magnetic field gradients, micro-vibration from the mechanical coolers [60, 163] and EMI from the satellite. The core of the FPA under development for X-IFU [52, 74, 163] consists of the large TES microcalorimeters array and its SQUID-based multiplexing cold readout electronics, plus a second TES array detector located at a close distance underneath the main array to be used as a cryogenic anti-coincidence detector [30, 101]. The latter shall reduce the particles background, induced by primary protons of both solar and cosmic rays origin, and secondary electrons, to a total level of  $< 5 \cdot 10^{-3}$  cts/cm<sup>2</sup>/s/keV in the 2–10 keV energy

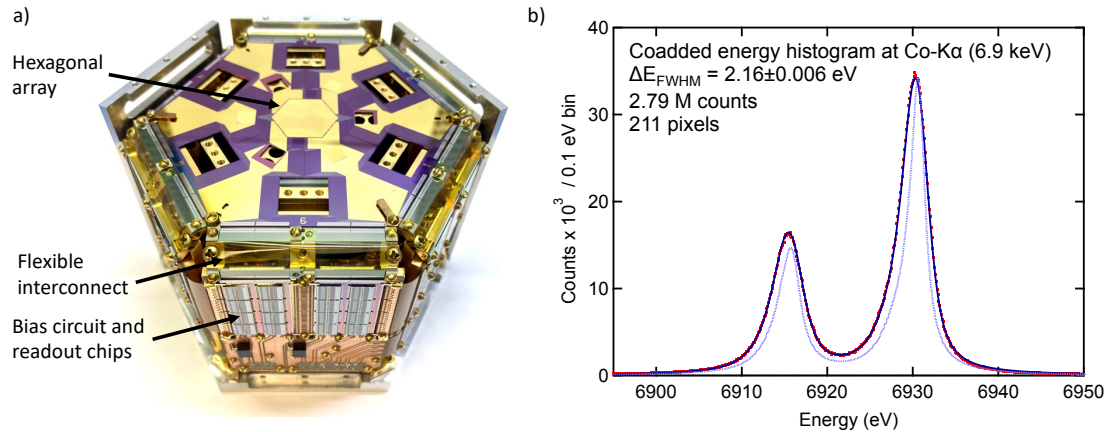


**Fig. 17** a) Photograph of a full scale 3k-pixel array being developed at NASA/GSFC for Athena/X-IFU (image provided courtesy of NASA/GSFC) b) Energy histogram including 200-pixels readout with TDM from a 1k prototype array demonstrating  $\Delta E_{FWHM} = 2.17$  eV for Co-K $\alpha$  X-rays (6.9 keV) [143]. The blue-dashed line is the natural line shape of the Co-K $\alpha$  complex, and the solid blue-line is the fit to the red data points.

band. The other key building blocks of the FPA consist of the detector assembly, the thermal suspension, the electromagnetic shielding, the FPA-internal wiring harness, the electronics assembly, and the thermal strapping. Critical to achieving high resolution with a TES X-ray spectrometer will be the shielding of the absolute static magnetic flux density component normal to the detector array surface, which needs to be less than  $1 \mu\text{T}$ , including any gradients across the whole array. Additionally, the maximum normal magnetic field noise over the detector surface should be less than  $20 \text{ pT}/\sqrt{\text{Hz}}$  within the signal bandwidth. These stringent requirements call for a careful design of magnetic shields that should provide a shielding factor of  $10^5$  or more [17].

Orders of magnitude larger format pixel arrays are envisaged for the future proposed X-ray missions beyond Athena. To implement arrays greater than the k-pixel scale to 10's, 100's k-pixels or even mega pixel arrays will require further maturation of both focal plane array and readout technologies. In addition to hydras, other advanced focal plane technologies are being developed that could enable and expand the capabilities of next generation X-ray microcalorimeter instruments. This includes the development of advanced fabrication techniques that enable detectors of different designs to be fabricated in a single focal plane array, as well as high-yield, high density wiring. Hybrid arrays may include pixels of different pitch, absorber composition and TES transition temperature (or shape) and thus enable the flexibility to design different parts of the focal plane to achieve different performance requirements [162, 172]. This could enable more efficient instruments with enhanced performance capabilities. For example a point-source array optimized for high angular resolution, high count-rate observations could be accompanied by an array to expand the field-of-view for diffuse observations. The use of hydras can alleviate some of the issues associated with routing of high-density array wiring within the focal-plane array. However, extremely fine ( $\leq 1 \mu\text{m}$ ), high yield wiring is particularly important where small pixel pitches are desired or when single pixel TESs are preferred over hydras [31]. Multi-stack wiring layers buried directly within a Si wafer has been demonstrated by several commercial foundries such as Massachusetts Institute of Technology Lincoln Laboratory (MIT/LL) [152, 171]. Multilayer technology may eventually enable other components like the bias (shunt resistors and inductors) and SQUID readout circuitry to be fabricated withing the same wafer as the detector. This may enable more compact focal-plane designs reducing the instrument mass (smaller focal-plane assemblies and magnetic shielding) or enable even larger arrays.

Readout technologies (see Chapter "Signal readout for Transition-Edge Sensor X-ray imaging spectrometers") are also rapidly advancing. Looking beyond current state of the art readouts such as time-domain-multiplexing (TDM) and low frequency-division-multiplexing (FDM), microwave (GHz) multiplexing ( $\mu\text{-mux}$ ) is a rapidly maturing technology and is already fielded in ground based instruments [104]. In  $\mu\text{-mux}$  each TES is coupled to an rf-SQUID and microwave resonator circuit. Each resonator is tuned to a dif-

ferent frequency and capacitively coupled to a single microwave feed-line. All pixels on the feed-line are then readout by a cryogenic amplifier such as a high-electron mobility transistor (HEMT). By moving the carrier signals to the GHz regime,  $\mu$ -mux dramatically increases the available bandwidth and allows many pixels to be read-out on a single microwave feed-line. HEMT amplifiers dissipate a significant amount of power and thus limit the number that can be implemented in a space instrument with finite available cooling power. Travelling-wave parametric amplifiers (TWPA) are promising alternatives to semiconductor amplifiers like HEMTs, with the potential to provide low noise amplification at 4K with significantly lower power dissipation [103]. Thus TWPA's have the potential to yet further increase the number of pixels that can be readout for future instruments.

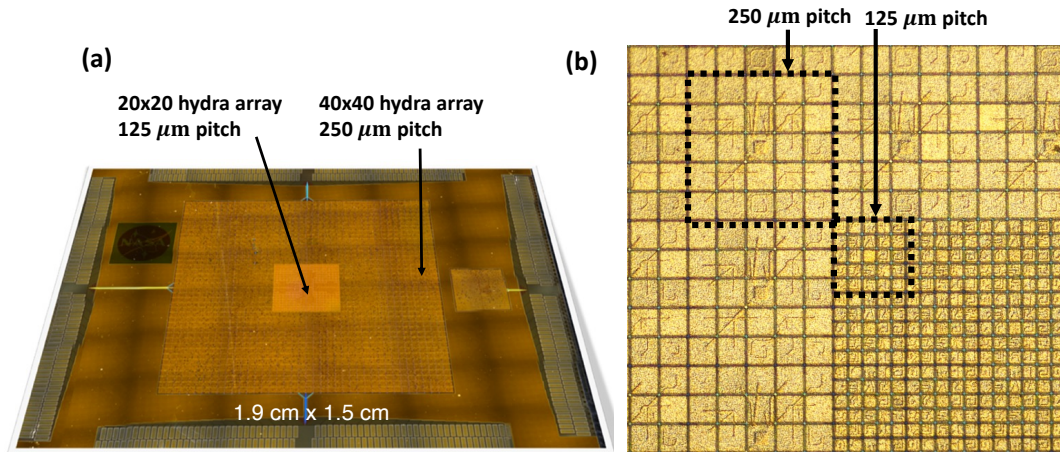


**Fig. 18** a) Photograph of a prototype 50-k pixel Lynx Microcalorimeter Array under development at NASA/GSFC [7]. b) Zoom-in photograph of part of the LXM test array including 125  $\mu\text{m}$  pitch Enhanced Main Array hydras in the central region of the array surrounded by a region of 250  $\mu\text{m}$  pitch Main Array hydras [142].

The Lynx X-ray telescope was a Flagship mission concept studied by NASA as part of the 2020 Astrophysics Decadal survey [51]. Although not selected to be the next Flagship, a Lynx-like mission was endorsed for further technology maturation and could launch sometime after 2040. The Lynx X-ray Microcalorimeter (LXM) is one of the main instruments that would combine a sub arc-second X-ray optic with a 100k-pixel array [7]. LXM is an example of a instrument that combines of many of the advance detector and readout concepts described above. LXM consist of a hybrid array of three different detectors on the same substrate. The LXM main array consists of 3456, 25-pixel hydras on a 50  $\mu\text{m}$  pitch (86k total pixels) with  $\Delta E_{FWHM} = 3$  eV at 0.2–7 keV. The main array provides a field-of-view of 5 arc-minutes and an angular resolution of 1 arc-second. The central 1 arc-minute region of the array consists 512, 25-pixel hydras with each pixel on a 25  $\mu\text{m}$  pitch (13k total pixels) [142]. This, enhanced main array will provide 0.5 arc-second imaging with  $\Delta E_{FWHM} = 2$  eV up to 7 keV. Finally, there is an ultra-high resolution subarray of 25  $\mu\text{m}$  single pixel TESs, optimized to achieve  $\Delta E_{FWHM} = 0.3$  eV up to 1 keV [128]. NASA/GSFC has developed a process to incorporate planarized, multi-stack buried wiring layers from Massachusetts Institute of Technology Lincoln Laboratory (MIT/LL) with their TES array design. The LXM detector will be read-out with  $\mu$ -mux and HEMT amplifiers [16]. By combining 25-pixel hydras that incorporate buried wiring, with state-of-the-art  $\mu$ -mux, it becomes practical to realize a 100k-pixel instrument within the engineering constraints of a satellite. Figure 18 shows a prototype LXM array that includes all three array types.

The Line Emission Mapper (LEM) is a probe-class mission concept under study by NASA for a possible launch in the 2030's [112]. LEM will combine a Si-shell mirror with an extremely large format microcalorimeter array to provide a  $\sim 30$  arc-minute field-of-view (FOV), 15 arc-second angular resolution, and  $\sim 2$  eV energy resolution. In contrast to ESA's Athena and NASA's Lynx concept, LEM will focus on large FOV science below 2 keV, such as the chemistry of the circumgalactic medium (CGM) and intergalactic medium (IGM). LEM's extremely large "grasp" (FOV x effective array) — enables the

mapping of faint extended sources such as IGM, GCM, 12 times more efficiently than Athena. The LEM microcalorimeter will consist of 4k, 4-pixel hydras (16k total imaging elements) and will be readout using TDM. A hybrid array configuration that includes the addition of a small sub-array of 1 eV resolution pixels is also under consideration.

The Super Diffuse Intergalactic Oxygen Surveyor (Super-DIOS) is mission concept under study in Japan (ISAS/JAXA) [129] with a possible launch after 2030. The satellite would perform wide field X-ray spectroscopy with a comparable FoV of about 0.5–1 deg, and with an angular resolution of  $\sim 15$  arc-seconds. The focal plane array will have 30k TESs read-out with  $\mu$ -mux, with resolution similar to X-IFU. The Cosmic Web Explorer (CWE) is a concept being proposed in Europe as part of ESA's Voyage-2050 program to survey the very faint warm-hot diffuse baryons in the local Universe [132]. CWE will have a mega-pixel array with resolving power of 3000 at 1 keV, comparable to the LXM ultra high resolution array, but with larger collecting area and angular resolution.

## References

- [1] Adams JS, Baker R, Bandler SR, Bastidon N, Danowski ME, Doriese WB, Eckart ME, Figueroa-Feliciano E, Goldfinger DC, Heine SNT, Hilton GC, Hubbard AJF, Kelley RL, Kilbourne CA, Manzagol-Harwood RE, McCammon D, Okajima T, Porter FS, Reintsema CD, Serlemitsos P, Smith SJ, Ullom JN, Wikus P (2020) First Operation of TES Microcalorimeters in Space with the Micro-X Sounding Rocket. *Journal of Low Temperature Physics* 199(3-4):1062–1071, DOI 10.1007/s10909-019-02293-5, [1908.09689](https://doi.org/10.1007/s10909-019-02293-5)
- [2] Ahmad K, Liu J, Liu Q, Li G, Liu J, Chen W (2019) Fabrication and Characterization of Superconducting Bilayer (Al/Ti) Transition-Edge Sensor Bolometer Array. *Journal of Electronic Materials* 48(2):925–929, DOI 10.1007/s11664-018-6806-4
- [3] Akamatsu H, Vaccaro D, Gottardi L, van der Kuur J, de Vries CP, Kiviranta M, Ravensberg K, D'Andrea M, Taralli E, de Wit M, Bruijn MP, van der Hulst P, den Hartog RH, van Leeuwen BJ, van der Linden AJ, McCalden AJ, Nagayoshi K, Nieuwenhuizen ACT, Ridder ML, Visser S, van Winden P, Gao JR, Hoogeveen RWM, Jackson BD, den Herder JWA (2021) Demonstration of MHz frequency domain multiplexing readout of 37 transition edge sensors for high-resolution x-ray imaging spectrometers. *Applied Physics Letters* 119(18):182601, DOI 10.1063/5.0066240, [2111.01797](https://doi.org/10.1063/5.0066240)
- [4] Anderson PW, Rowell JM (1963) Probable observation of the Josephson superconducting tunneling effect. *Phys Rev Lett* 10:230–232, DOI 10.1103/PhysRevLett.10.230, URL <https://link.aps.org/doi/10.1103/PhysRevLett.10.230>
- [5] Aslamazov LG, Larkin AI (1969) Josephson effect in superconducting point contacts. *JETP Lett (USSR)* 9
- [6] Bandler SR, Brekosky RP, Brown AD, Chervenak JA, Figueroa-Feliciano E, Finkbeiner FM, Iyomoto N, Kelley RL, Kilbourne CA, Porter FS, Sadleir J, Smith SJ (2008) Performance of TES X-ray Microcalorimeters with a Novel Absorber Design. *Journal of Low Temperature Physics* 151(1-2):400–405, DOI 10.1007/s10909-007-9673-6
- [7] Bandler SR, Chervenak JA, Datesman AM, Devasia AM, DiPirro M, Sakai K, Smith SJ, Stevenson TR, Yoon W, Bennett D, Mates B, Swetz D, Ullom JN, Irwin KD, Eckart ME, Figueroa-Feliciano E, McCammon D, Ryu K, Olson J, Zeiger B (2019) Lynx x-ray microcalorimeter. *Journal of Astronomical Telescopes, Instruments, and Systems* 5:021017, DOI 10.1117/1.JATIS.5.2.021017
- [8] Barbera M, Cicero UL, Sciortino L, D'Anca F, Cicero GL, Parodi G, Sciortino S, Rauw G, Branduardi-Raymont G, Varisco S, Bonura SF, Collura A, Candia R, Cicca GD, Giglio P, Buttacavoli A, Cuttaia F, Villa F, Cappi M, Trong TL, Mesnager JM, Peille P, den Hartog R, den Herder JW, Jackson B, Barret D, Piro L (2018) ATHENA X-IFU thermal filters development status toward the end of the instrument phase-A. In: den Herder JWA, Nikzad S, Nakazawa K (eds) *Space Telescopes and Instrumentation 2018: Ultraviolet to Gamma Ray*, International Society for Optics and Photonics, SPIE, vol 10699, pp 406 – 420, DOI 10.1117/12.2314450, URL <https://doi.org/10.1117/12.2314450>



- [9] Bardeen J, Cooper LN, Schrieffer JR (1957) Microscopic Theory of Superconductivity. *Physical Review* 106(1):162–164, DOI 10.1103/PhysRev.106.162
- [10] Barone A, Paterno Gianfranco VL (1982) John Wiley & Sons, Ltd. DOI <https://doi.org/10.1002/>, URL <https://onlinelibrary.wiley.com/doi/abs/10.1002/>, <https://onlinelibrary.wiley.com/doi/pdf/10.1002/>
- [11] Barret D, Trong TL, den Herder JW, Piro L, Cappi M, Houvelin J, Kelley R, et al. (2018) The ATHENA X-ray Integral Field Unit (X-IFU). In: den Herder JWA, Nikzad S, Nakazawa K (eds) *Space Telescopes and Instrumentation 2018: Ultraviolet to Gamma Ray*, International Society for Optics and Photonics, SPIE, vol 10699, pp 324 – 338, DOI 10.1117/12.2312409, URL <https://doi.org/10.1117/12.2312409>
- [12] Bennett DA, Horansky RD, Hoover AS, Hotelling NJ, Rabin MW, Schmidt DR, Swetz DS, Vale LR, Ullom JN (2010) An analytical model for pulse shape and electrothermal stability in two-body transition-edge sensor microcalorimeters. *Applied Physics Letters* 97(10):102504, DOI 10.1063/1.3486477
- [13] Bennett DA, Swetz DS, Horansky RD, Schmidt DR, Ullom JN (2012) A Two-Fluid Model for the Transition Shape in Transition-Edge Sensors. *Journal of Low Temperature Physics* 167(3-4):102–107, DOI 10.1007/s10909-011-0431-4
- [14] Bennett DA, Swetz DS, Schmidt DR, Ullom JN (2013) Resistance in transition-edge sensors: A comparison of the resistively shunted junction and two-fluid models. *Phys Rev B* 87:020508, DOI 10.1103/PhysRevB.87.020508
- [15] Bennett DA, Schmidt DR, Swetz DS, Ullom JN (2014) Phase-slip lines as a resistance mechanism in transition-edge sensors. *Applied Physics Letters* 104(4):042602, DOI 10.1063/1.4863664
- [16] Bennett DA, Mates JAB, Bandler SR, Becker DT, Fowler JW, Gard JD, Hilton GC, Irwin KD, Morgan KM, Reintsema CD, Sakai K, Schmidt DR, Smith SJ, Swetz DS, Ullom JN, Vale LR, Wessels AL (2019) Microwave SQUID multiplexing for the Lynx x-ray microcalorimeter. *Journal of Astronomical Telescopes, Instruments, and Systems* 5:021007, DOI 10.1117/1.JATIS.5.2.021007
- [17] Bergen A, van Weers HJ, Bruineman C, Dhallé MMJ, Krooshoop HJG, ter Brake HJM, Ravensberg K, Jackson BD, Wafelbakker CK (2016) Design and validation of a large-format transition edge sensor array magnetic shielding system for space application. *Review of Scientific Instruments* 87(10):105109, DOI 10.1063/1.4962157, URL <https://doi.org/10.1063/1.4962157>, <https://doi.org/10.1063/1.4962157>
- [18] Boyce KR, Audley MD, Baker RG, Dumonthier JJ, Fujimoto R, Gendreau KC, Ishisaki Y, Kelley RL, Stahle CK, Szymkowiak AE, Winkert GE (1999) Design and performance of the ASTRO-E/XRS signal processing system. In: Siegmund OH, Flanagan KA (eds) *EUV, X-Ray, and Gamma-Ray Instrumentation for Astronomy X*, Society of Photo-Optical Instrumentation Engineers (SPIE) Conference Series, vol 3765, pp 741–750, DOI 10.1117/12.366557
- [19] Boyle WS, Rodgers KF (1959) Performance characteristics of a new low-temperature bolometer. *J Opt Soc Am* 49(1):66–69, DOI 10.1364/JOSA.49.000066, URL <http://opg.optica.org/abstract.cfm?URI=josa-49-1-66>
- [20] Brown AD, Bandler SR, Brekosky R, Chervenak JA, Figueroa-Feliciano E, Finkbeiner F, Iyomoto N, Kelley RL, Kilbourne CA, Porter FS, Smith S, Saab T, Sadleir J (2008) Absorber Materials for Transition-Edge Sensor X-ray Microcalorimeters. *J Low Temp Phys* 151(1-2):413–417, DOI 10.1007/s10909-007-9669-2
- [21] Brown GV, Beiersdorfer P, Chen H, Scofield JH, Boyce KR, Kelley RL, Kilbourne CA, Porter FS, Gu MF, Kahn SM, Szymkowiak AE (2006) Energy-dependent excitation cross section measurements of the diagnostic lines of Fe XVII. *Phys Rev Lett* 96:253201, DOI 10.1103/PhysRevLett.96.253201, URL <https://link.aps.org/doi/10.1103/PhysRevLett.96.253201>
- [22] Bruijn M, van der Linden A, Ferrari L, Gottardi L, van der Kuur J, den Hartog R, Akamatsu H, Jackson B (2018) Lc filters for fdm readout of the x-ifu tes calorimeter instrument on athena. *J Low Temp Phys* 193:661–667
- [23] Bruijn MP, Gottardi L, den Hartog RH, van der Kuur J, van der Linden AJ, Jackson BD (2014) Tailoring the high-q lc filter arrays for readout of kilo-pixel tes arrays in the spica-safari instrument. *J Low Temp Phys* 176:421–425

- [24] Busch SE, Adams JS, Bandler SR, Chervenak JA, Eckart ME, Finkbeiner FM, Fixsen DJ, Kelley RL, Kilbourne CA, Lee SJ, Moseley SH, Porst JP, Porter FS, Sadleir JE, Smith SJ (2016) Progress Towards Improved Analysis of TES X-ray Data Using Principal Component Analysis. *Journal of Low Temperature Physics* 184(1-2):382–388, DOI 10.1007/s10909-015-1357-z
- [25] Chervenak JA, Finkbeiner FM, Bandler SR, Brekosky R, Brown AD, Iyomoto N, Kelley RL, Kilbourne CA, Porter FS, Sadleir J, Smith S (2008) Materials Development for Auxiliary Components for Large Compact Mo/Au TES Arrays. *Journal of Low Temperature Physics* 151(1-2):255–260, DOI 10.1007/s10909-007-9636-y
- [26] Coffey WT, Kalmykov YP, Titov SV, Cleary L (2008) Smoluchowski equation approach for quantum brownian motion in a tilted periodic potential. *Phys Rev E* 78:031114, DOI 10.1103/PhysRevE.78.031114, URL <https://link.aps.org/doi/10.1103/PhysRevE.78.031114>
- [27] Cucchetti E, Eckart ME, Peille P, Porter FS, Pajot F, Pointecouteau E (2018) Multi-parameter Non-linear Gain Correction of X-ray Transition Edge Sensors for the X-ray Integral Field Unit. *Journal of Low Temperature Physics* 193(5-6):931–939, DOI 10.1007/s10909-018-1912-5
- [28] Cucchetti E, Eckart ME, Peille P, de Vries C, Pajot F, Pointecouteau E, Leutenegger M, Kilbourne CA, Porter FS (2018) Energy scale calibration and drift correction of the X-IFU. In: den Herder JWA, Nikzad S, Nakazawa K (eds) *Space Telescopes and Instrumentation 2018: Ultraviolet to Gamma Ray*, International Society for Optics and Photonics, SPIE, vol 10699, pp 1130 – 1140, DOI 10.1117/12.2312170, URL <https://doi.org/10.1117/12.2312170>
- [29] Cucchetti E, Pajot F, Pointecouteau E, Peille P, Betancourt-Martinez G, Smith SJ, Barbera M, Eckart ME, Bandler SR, Kilbourne CA, Cappi M, Barret D (2018) Testing the X-IFU calibration requirements: an example for quantum efficiency and energy resolution. In: den Herder JWA, Nikzad S, Nakazawa K (eds) *Space Telescopes and Instrumentation 2018: Ultraviolet to Gamma Ray*, International Society for Optics and Photonics, SPIE, vol 10699, pp 1152 – 1160, DOI 10.1117/12.2312188, URL <https://doi.org/10.1117/12.2312188>
- [30] D’Andrea M, Macculi C, Argan A, Lotti S, Minervini G, Piro L, Biasotti M, Ceriale V, Gallucci G, Gatti F, Torrioli G, Volpe A (2018) The cryogenic anticoincidence detector for ATHENA X-IFU: preliminary test of AC-S9 towards the demonstration model. In: den Herder JWA, Nikzad S, Nakazawa K (eds) *Space Telescopes and Instrumentation 2018: Ultraviolet to Gamma Ray*, Society of Photo-Optical Instrumentation Engineers (SPIE) Conference Series, vol 10699, p 106994T, DOI 10.1117/12.2313280, [1807.02344](https://doi.org/10.1117/12.2313280)
- [31] Datesman AM, Adams JS, Bandler SR, Betancourt-Martinez GL, Chang MP, Chervenak JA, Eckart ME, Ewin AE, Finkbeiner FM, Ha JY, Kelley RL, Kilbourne CA, Miniussi AR, Porter FS, Sadleir JE, Sakai K, Smith SJ, Wakeham NA, Williams EH, Wassell EJ, Yoon W (2017) Reduced-Scale Transition-Edge Sensor Detectors for Solar and X-Ray Astrophysics. *IEEE Transactions on Applied Superconductivity* 27(4):2649839, DOI 10.1109/TASC.2017.2649839
- [32] Davis JC, Packard RE (2002) Superfluid  $^3\text{He}$  josephson weak links. *Rev Mod Phys* 74:741–773, DOI 10.1103/RevModPhys.74.741, URL <https://link.aps.org/doi/10.1103/RevModPhys.74.741>
- [33] de Vries CP, Schouten RM, van der Kuur J, Gottardi L, Akamatsu H (2016) Microcalorimeter pulse analysis by means of principle component decomposition. In: den Herder JWA, Takahashi T, Bautz M (eds) *Space Telescopes and Instrumentation 2016: Ultraviolet to Gamma Ray*, Society of Photo-Optical Instrumentation Engineers (SPIE) Conference Series, vol 9905, p 99055V, DOI 10.1117/12.2231627, [1607.00834](https://doi.org/10.1117/12.2231627)
- [34] de Wit M, Gottardi L, Taralli E, Nagayoshi K, Ridder ML, Akamatsu H, Bruijn MP, Hoogeveen RWM, van der Kuur J, Ravensberg K, Vaccaro D, Gao JR, den Herder JWA (2021) Impact of the Absorber-Coupling Design for Transition-Edge-Sensor X-Ray Calorimeters. *Physical Review Applied* 16(4):044059, DOI 10.1103/PhysRevApplied.16.044059, [2107.09552](https://doi.org/10.1103/PhysRevApplied.16.044059)
- [35] de Wit M, Gottardi L, Ridder ML, Nagayoshi K, Taralli E, Akamatsu H, Vaccaro D, den Herder JWA, Bruijn MP, Gao JR (2022) Mitigation of the Magnetic Field Susceptibility of Transition-Edge Sensors Using a Superconducting Groundplane. *Physical Review Applied* 18(2):024066, DOI 10.1103/PhysRevApplied.18.024066, [2208.10775](https://doi.org/10.1103/PhysRevApplied.18.024066)
- [36] Doriese WB, Adams JS, Hilton GC, Irwin KD, Kilbourne CA, Schima FJ, Ullom JN (2009) Optimal filtering, record length, and count rate in transition-edge-sensor microcalorimeters.

- AIP Conference Proceedings 1185(1):450–453, DOI 10.1063/1.3292375, URL <https://aip.scitation.org/doi/abs/10.1063/1.3292375>, <https://aip.scitation.org/doi/pdf/10.1063/1.3292375>
- [37] Doriese WB, Abbamonte P, Alpert BK, Bennett DA, Denison EV, Fang Y, Fischer DA, Fitzgerald CP, Fowler JW, Gard JD, Hays-Wehle JP, Hilton GC, Jaye C, McChesney JL, Miaja-Avila L, Morgan KM, Joe YI, O’Neil GC, Reintsema CD, Rodolakis F, Schmidt DR, Tatsuno H, Uhlig J, Vale LR, Ullom JN, Swetz DS (2017) A practical superconducting-microcalorimeter X-ray spectrometer for beamline and laboratory science. *Review of Scientific Instruments* 88(5):053108, DOI 10.1063/1.4983316
- [38] Eckart ME, Adams JS, Boyce KR, Brown GV, Chiao MP, Fujimoto R, Haas DA, den Herder JWA, Hoshino A, Ishisaki Y, Kilbourne CA, Kitamoto S, Leutenegger MA, McCammon D, Mitsuda K, Porter FS, Sato K, Sawada M, Seta H, Sneiderman GA, Szymkowiak AE, Takei Y, Tashiro MS, Tsujimoto M, de Vries CP, Watanabe T, Yamada S, Yamasaki NY (2018) Ground calibration of the Astro-H (Hitomi) soft x-ray spectrometer. *Journal of Astronomical Telescopes, Instruments, and Systems* 4(2):1 – 22, DOI 10.1117/1.JATIS.4.2.021406, URL <https://doi.org/10.1117/1.JATIS.4.2.021406>
- [39] Eckart ME, Adams JS, Bandler SR, Beaumont S, Chervenak JA, Datesman AM, Finkbeiner FM, Hummatov R, Kelley RL, Kilbourne CA, Leutenegger MA, Miniussi AR, Moseley SJ, Porter FS, Sadleir JE, Sakai K, Smith SJ, Wakeham NA, Wassell EJ (2019) Extended Line Spread Function of TES Microcalorimeters With Au/Bi Absorbers. *IEEE Transactions on Applied Superconductivity* 29(5):2903420, DOI 10.1109/TASC.2019.2903420
- [40] Fabrega L, Fernandez-Martinez I, Gil O, Parra-Borderias M, Camon A, Costa-Kramer J, Gonzalez-Arrabal R, Sese J, Briones F, Santiso J, Peiro F (2009) Mo-based proximity bilayers for tes: Microstructure and properties. *IEEE Transactions on Applied Superconductivity* 19(3):460–464, DOI 10.1109/TASC.2009.2019052
- [41] Feynman RP (1957) Superfluidity and superconductivity. *Rev Mod Phys* 29(2):205–212, DOI <https://doi.org/10.1103/RevModPhys.29.205>
- [42] Figueroa-Feliciano E (2004) Position-sensitive low-temperature detectors. *Nuclear Instruments and Methods in Physics Research Section A: Accelerators, Spectrometers, Detectors and Associated Equipment* 520(1):496–501, DOI <https://doi.org/10.1016/j.nima.2003.11.297>, URL <https://www.sciencedirect.com/science/article/pii/S0168900203032194>, proceedings of the 10th International Workshop on Low Temperature Detectors
- [43] Finkbeiner FM, Adams JS, Bandler SR, Betancourt-Martinez GL, Brown AD, Chang MP, Chervenak JA, Chiao MP, Datesman AM, Eckart ME, Kelley RL, Kilbourne CA, Miniussi AR, Moseley SJ, Porter FS, Sadleir JE, Sakai K, Smith SJ, Wakeham NA, Wassell EJ, Yoon W (2017) Electron-Beam Deposition of Superconducting Molybdenum Thin Films for the Development of Mo/Au TES X-ray Microcalorimeter. *IEEE Transactions on Applied Superconductivity* 27(4):2633785, DOI 10.1109/TASC.2016.2633785
- [44] Fixsen DJ, Moseley SH, Cabrera B, Figueroa-Feliciano E (2004) Pulse estimation in nonlinear detectors with nonstationary noise. *Nuclear Instruments and Methods in Physics Research A* 520(1-3):555–558, DOI 10.1016/j.nima.2003.11.313
- [45] Fowler JW, Alpert BK, Doriese WB, Fischer DA, Jaye C, Joe YI, O’Neil GC, Swetz DS, Ullom JN (2015) MICROCALORIMETER SPECTROSCOPY AT HIGH PULSE RATES: A MULTI-PULSE FITTING TECHNIQUE. *The Astrophysical Journal Supplement Series* 219(2):35, DOI 10.1088/0067-0049/219/2/35, URL <https://doi.org/10.1088/0067-0049/219/2/35>
- [46] Fowler JW, Alpert BK, Doriese WB, Joe YI, O’Neil GC, Ullom JN, Swetz DS (2016) The Practice of Pulse Processing. *Journal of Low Temperature Physics* 184(1-2):374–381, DOI 10.1007/s10909-015-1380-0, [1511.03950](https://doi.org/10.1007/s10909-015-1380-0)
- [47] Fowler JW, Alpert BK, Doriese WB, Hays-Wehle J, Joe YI, Morgan KM, O’Neil GC, Reintsema CD, Schmidt DR, Ullom JN, Swetz DS (2017) When “Optimal Filtering” Isn’t. *IEEE Transactions on Applied Superconductivity* 27(4):2637359, DOI 10.1109/TASC.2016.2637359
- [48] Fowler JW, Pappas CG, Alpert BK, Doriese WB, O’Neil GC, Ullom JN, Swetz DS (2018) Approaches to the Optimal Nonlinear Analysis of Microcalorimeter Pulses. *Journal of Low Temperature Physics* 193(3-4):539–546, DOI 10.1007/s10909-018-1892-5, [1803.02827](https://doi.org/10.1007/s10909-018-1892-5)

- [49] Fowler JW, Alpert BK, Joe YI, O’Neil GC, Swetz DS, Ullom JN (2020) A Robust Principal Component Analysis for Outlier Identification in Messy Microcalorimeter Data. *Journal of Low Temperature Physics* 199(3-4):745–753, DOI 10.1007/s10909-019-02248-w, [1911.00423](https://doi.org/10.1007/s10909-019-02248-w)
- [50] Gall AC, Dipti, Buechele SW, Sanders S, Szabo CI, Silwal R, Ralchenko Y, Brickhouse N, Takacs E (2020) Measurements of linear polarization of satellite transitions from Li- and Be-like Ar ions. *J Phys B Atom Molec Phys* 53(14):145004, DOI 10.1088/1361-6455/ab8eff
- [51] Gaskin JA, Swartz DA, Vikhlinin A, Özel F, Gelmis KE, Arenberg JW, Bandler SR, Bautz MW, Civitani MM, Dominguez A, Eckart ME, Falcone AD, Figueroa-Feliciano E, Freeman MD, Günther HM, Havey KA, Heilmann RK, Kilaru K, Kraft RP, McCarley KS, McEntaffer RL, Pareschi G, Purcell W, Reid PB, Schattenburg ML, Schwartz DA, Schwartz ED, Tananbaum HD, Tremblay GR, Zhang WW, Zuhone JA (2019) Lynx X-Ray Observatory: an overview. *Journal of Astronomical Telescopes* 5:021001, DOI 10.1117/1.JATIS.5.2.021001
- [52] Geoffroy H, Jackson B, Bandler S, Doriese WB, Kirivanta M, Prêle D, Ravera L, Argan A, Barbera M, van der Kuur J, van Leeuwen BJ, van Weers H, Hooegeveen R, den Herder JW, Smith S, Adams J, Chervenak J, Durkin M, Reintsema C, Ullom J, Parot Y, Barret D, Macculi C, Piro L, Brachet F, Ledot A (2020) Conceptual design of the detection chain for the X-IFU on Athena. In: den Herder JWA, Nikzad S, Nakazawa K (eds) *Space Telescopes and Instrumentation 2020: Ultraviolet to Gamma Ray*, International Society for Optics and Photonics, SPIE, vol 11444, DOI 10.1117/12.2563628, URL <https://doi.org/10.1117/12.2563628>
- [53] Goldie DJ, Audley MD, Glowacka DM, Tsaneva VN, Withington S (2009) Thermal models and noise in transition edge sensors. *Journal of Applied Physics* 105(7):074512, DOI 10.1063/1.3097396, <https://doi.org/10.1063/1.3097396>
- [54] Golubov AA, Kupriyanov MY, Il’ichev E (2004) The current-phase relation in josephson junctions. *Rev Mod Phys* 76:411–469, DOI 10.1103/RevModPhys.76.411, URL <https://link.aps.org/doi/10.1103/RevModPhys.76.411>
- [55] Gottardi L, Nagayashi K (2021) A review of x-ray microcalorimeters based on superconducting transition edge sensors for astrophysics and particle physics. *Applied Sciences* 11:3793
- [56] Gottardi L, Kozorezov A, Akamatsu H, van der Kuur J, Bruijn MP, den Hartog RH, Hijmering R, Khosropanah P, Lambert C, van der Linden AJ, Ridder ML, Suzuki T, Gao JR (2014) Josephson effects in an alternating current biased transition edge sensor. *Appl Phys Lett* 105(16):162605
- [57] Gottardi L, Akamatsu H, van der Kuur J, Smith SJ, Kozorezov A, Chervenak J (2017) Study of tes-based microcalorimeters of different size and geometry under ac bias. *IEEE Transactions on Applied Superconductivity* 27(4):1–4, DOI 10.1109/TASC.2017.2655500
- [58] Gottardi L, Smith S, Kozorezov A, et al. (2018) Josephson effects in frequency-domain multiplexed tes microcalorimeters and bolometers. *J Low Temp Phys* 193:209–216
- [59] Gottardi L, van der Kuur J, Bruijn M, van der Linden A, Kiviranta M, Akamatsu H, den Hartog R, Ravensberg K (2019) Intrinsic losses and noise of high-q lithographic mhz lc resonators for frequency division multiplexing. *J Low Temp Phys* 194:370–376
- [60] Gottardi L, van Weers H, Dercksen J, Akamatsu H, Bruijn MP, Gao JR, Jackson B, Khosropanah P, van der Kuur J, Ravensberg K, Ridder ML (2019) A six-degree-of-freedom micro-vibration acoustic isolator for low-temperature radiation detectors based on superconducting transition-edge sensors. *Review of Scientific Instruments* 90(5):055107, DOI 10.1063/1.5088364
- [61] Gottardi L, de Wit M, Taralli E, Nagayashi K, Kozorezov A (2021) Voltage Fluctuations in ac Biased Superconducting Transition-Edge Sensors. *Phys Rev Lett* 126(21):217001, DOI 10.1103/PhysRevLett.126.217001
- [62] Hays-Wehle JP, Schmidt DR, Ullom JN, Swetz DS (2016) Thermal Conductance Engineering for High-Speed TES Microcalorimeters. *Journal of Low Temperature Physics* 184(1-2):492–497, DOI 10.1007/s10909-015-1416-5
- [63] Hitomi Collaboration, Aharonian F, Akamatsu H, Akimoto F, Allen SW, Anabuki N, Angelini L, Arnaud K, Audard M, Awaki H, Axelsson M, Bamba A, Bautz M, Blandford R, Brenneman L, Brown GV, Bulbul E, Cackett E, Chernyakova M, Chiao M, Coppi P, Costantini E, de Plaa J, den Herder JW, Done C, Dotani T, Ebisawa K, Eckart M, Enoto T, Ezoe Y, Fabian AC, Ferrigno C, Foster A, Fujimoto R, Fukazawa Y, Furuzawa A, Galeazzi M, Gallo L, Gandhi P, Giustini M, Goldwurm A, Gu L, Guainazzi M, Haba Y, Hagino K, Hamaguchi K, Harrus I, Hatsukade I, Hayashi K, Hayashi

- T, Hayashida K, Hiraga J, Hornschemeier A, Hoshino A, Hughes J, Iizuka R, Inoue H, Inoue Y, Ishibashi K, Ishida M, Ishikawa K, Ishisaki Y, Itoh M, Iyomoto N, Kaastra J, Kallman T, Kamae T, Kara E, Kataoka J, Katsuda S, Katsuta J, Kawaharada M, Kawai N, Kelley R, Khangulyan D, Kilbourne C, King A, Kitaguchi T, Kitamoto S, Kitayama T, Kohmura T, Kokubun M, Koyama S, Koyama K, Kretschmar P, Krimm H, Kubota A, Kunieda H, Laurent P, Lebrun F, Lee SH, Leutenegger M, Limousin O, Loewenstein M, Long KS, Lumb D, Madejski G, Maeda Y, Maier D, Makishima K, Markevitch M, Matsumoto H, Matsushita K, McCammon D, McNamara B, Mehdipour M, Miller E, Miller J, Mineshige S, Mitsuda K, Mitsuishi I, Miyazawa T, Mizuno T, Mori H, Mori K, Moseley H, Mukai K, Murakami H, Murakami T, Mushotzky R, Nagino R, Nakagawa T, Nakajima H, Nakamori T, Nakano T, Nakashima S, Nakazawa K, Nobukawa M, Noda H, Nomachi M, O'Dell S, Odaka H, Ohashi T, Ohno M, Okajima T, Ota N, Ozaki M, Paerels F, Paltani S, Parmar A, Petre R, Pinto C, Pohl M, Porter FS, Pottschmidt K, Ramsey B, Reynolds C, Russell H, Safi-Harb S, Saito S, Sakai K, Sameshima H, Sato G, Sato K, Sato R, Sawada M, Schartel N, Serlemitsos P, Seta H, Shidatsu M, Simionescu A, Smith R, Soong Y, Stawarz L, Sugawara Y, Sugita S, Szymkowiak A, Tajima H, Takahashi H, Takahashi T, Takeda S, Takei Y, Tamagawa T, Tamura K, Tamura T, Tanaka T, Tanaka Y, Tanaka Y, Tashiro M, Tawara Y, Terada Y, Terashima Y, Tombesi F, Tomida H, Tsuboi Y, Tsujimoto M, Tsunemi H, Tsuru T, Uchida H, Uchiyama H, Uchiyama Y, Ueda S, Ueda Y, Ueno S, Uno S, Urry M, Ursino E, de Vries C, Watanabe S, Werner N, Wik D, Wilkins D, Williams B, Yamada S, Yamaguchi H, Yamaoka K, Yamasaki NY, Yamauchi M, Yamauchi S, Yaqoob T, Yatsu Y, Yonetoku D, Yoshida A, Yuasa T, Zhuravleva I, Zoghbi A (2016) The quiescent intracluster medium in the core of the Perseus cluster. *Nature* 535(7610):117–121, DOI 10.1038/nature18627, [1607.04487](https://doi.org/10.1038/nature18627)
- [64] Hoevers HFC, Bento AC, Bruijn MP, Gottardi L, Korevaar MAN, Mels WA, de Korte PAJ (2000) Thermal fluctuation noise in a voltage biased superconducting transition edge thermometer. *Appl Phys Lett* 77(26):4422–4424
- [65] Hoevers HFC, Ridder ML, Germeau A, Bruijn MP, de Korte PAJ, Wiegerink RJ (2005) Radiative ballistic phonon transport in silicon-nitride membranes at low temperatures. *Applied Physics Letters* 86(25):251903, DOI 10.1063/1.1949269, URL <https://doi.org/10.1063/1.1949269>, <https://doi.org/10.1063/1.1949269>
- [66] Hollerith C, Simmnacher B, Weiland R, Feilitzsch Fv, Isaila C, Jochum J, Potzel W, Höhne J, Phelan K, Wernicke D, May T (2006) Energy calibration of superconducting transition edge sensors for x-ray detection using pulse analysis. *Review of Scientific Instruments* 77(5):053105-053105-6, DOI 10.1063/1.2202911
- [67] Hubmayr J, Austermann JE, Beall JA, Becker D, Bennett DA, Benson BA, Bleem LE, Chang CL, Carlstrom JE, Cho H, Crites AT, Dobbs M, Everett W, George EM, Holzapfel WL, Halverson NW, Henning JW, Hilton GC, Irwin KD, Li D, Lowell P, Lueker M, McMahan J, Mehl J, Meyer SS, Nibarger JP, Niemack MD, Schmidt DR, Shirokoff E, Simon SM, Yoon KW, Young EY (2011) Stability of al-mn transition edge sensors for frequency domain multiplexing. *IEEE Transactions on Applied Superconductivity* 21(3):203–206, DOI 10.1109/TASC.2010.2090630
- [68] Hummatov R, Adams JS, Bandler SR, Barlis A, Beaumont S, Chang MP, Chervenak JA, Datesman AM, Eckart ME, Finkbeiner FM, Ha JY, Kelley RL, Kilbourne CA, Miniussi AR, Porter FS, Sadleir JE, Sakai K, Smith SJ, Wakeham N, Wassell EJ, Wollack EJ (2020) Quantum Efficiency Study and Reflectivity Enhancement of Au/Bi Absorbers. *Journal of Low Temperature Physics* 199(1-2):393–400, DOI 10.1007/s10909-020-02424-3
- [69] Irwin K (2006) Thermodynamics of nonlinear bolometers near equilibrium. *Nucl Instrum and Methods Phys Res Sect A* 559(2):718 – 720
- [70] Irwin K, Hilton G (2005) *Transition-Edge Sensors*, Springer Berlin Heidelberg, Berlin, Heidelberg, pp 63–150. DOI 10.1007/10933596\_3, URL [https://doi.org/10.1007/10933596\\_3](https://doi.org/10.1007/10933596_3)
- [71] Irwin KD (1995) An application of electrothermal feedback for high resolution cryogenic particle detection. *Appl Phys Lett* 66(15):1998–2000
- [72] Irwin KD, Chaudhuri S, Cho HM, Dawson C, Kuenstner S, Li D, Titus CJ, Young BA (2018) A Spread-Spectrum SQUID Multiplexer. *Journal of Low Temperature Physics* 193(3-4):476–484, DOI 10.1007/s10909-018-1987-z, [1806.02805](https://doi.org/10.1007/s10909-018-1987-z)

- [73] Iyomoto N, Bandler S, Brekosky R, Chervenak J, Figueroa-Feliciano E, Finkbeiner F, Kelley R, Kilbourne C, Lindeman M, Murphy K, Porter F, Saab T, Sadleir J, Talley D (2006) Position-sensitive transition-edge sensors. *Nuclear Instruments and Methods in Physics Research Section A: Accelerators, Spectrometers, Detectors and Associated Equipment* 559(2):491–493, DOI <https://doi.org/10.1016/j.nima.2005.12.082>, URL <https://www.sciencedirect.com/science/article/pii/S0168900205025106>, proceedings of the 11th International Workshop on Low Temperature Detectors
- [74] Jackson BD, van Weers H, van der Kuur J, den Hartog R, Akamatsu H, Argan A, Bandler SR, Barbera M, Barret D, Bruijn MP, Chervenak JA, Dercksen J, Gatti F, Gottardi L, Haas D, den Herder JW, Kilbourne CA, Kiviranta M, Lam-Trong T, van Leeuwen BJ, Macculi C, Piro L, Smith SJ (2016) The focal plane assembly for the Athena X-ray Integral Field Unit instrument. In: den Herder JWA, Takahashi T, Bautz M (eds) *Space Telescopes and Instrumentation 2016: Ultraviolet to Gamma Ray*, Society of Photo-Optical Instrumentation Engineers (SPIE) Conference Series, vol 9905, p 99052I, DOI 10.1117/12.2232544
- [75] Jethava N, Ullom JN, Irwin KD, Doriese WB, Beall JA, Hilton GC, Vale LR, Zink B (2009) Dependence of excess noise on the partial derivatives of resistance in superconducting transition edge sensors. *AIP Conference Proceedings* 1185(1):31–33, DOI 10.1063/1.3292343
- [76] Josephson BD (1962) Possible new effects in superconductive tunnelling. *Physics Letters* 1(7):251–253, DOI 10.1016/0031-9163(62)91369-0
- [77] Kammoun ES, Barret D, Peille P, Willingale R, Dauser T, Wilms J, Guainazzi M, Miller JM (2022) The defocused observations of bright sources with Athena/X-IFU. arXiv e-prints arXiv:2205.01126, [2205.01126](https://arxiv.org/abs/2205.01126)
- [78] Kinnunen KM, Palosaari MRJ, Maasilta IJ (2012) Normal metal-superconductor decoupling as a source of thermal fluctuation noise in transition-edge sensors. *J Appl Phys* 112(3):034515
- [79] Kirsch C, Gottardi L, Lorenz M, Dauser T, den Hartog R, Jackson B, Peille P, Smith S, Wilms J (2020) Time-domain modeling of tes microcalorimeters under ac bias. *J Low Temp Phys* 199:569–576
- [80] Kiviranta M, Seppä H, van der Kuur J, de Korte P (2002) Squid-based readout schemes for microcalorimeter arrays. *AIP Conference Proceedings* 605(1):295–300, DOI 10.1063/1.1457649
- [81] Koch RH, Van Harlingen DJ, Clarke J (1980) Quantum-noise theory for the resistively shunted josephson junction. *Phys Rev Lett* 45:2132–2135, DOI 10.1103/PhysRevLett.45.2132, URL <https://link.aps.org/doi/10.1103/PhysRevLett.45.2132>
- [82] Kogan SM, Nagaev K (1988) *Zh Eksp Teor Fiz* 94:262
- [83] Kozorezov A, Golubov AA, Martin D, de Korte P, Lindeman M, Hijmering R, van der Kuur J, Hoevers H, Gottardi L, Kupriyanov M, Wigmore J (2011) *Appl Phys Lett* 99:063503
- [84] Kozorezov A, Golubov A, Martin D, de Korte P, Lindeman M, Hijmering R, van der Kuur J, Hoevers H, Gottardi L, Kupriyanov M, JK W (2012) Electrical noise in a tes as a resistively shunted conducting junction. *J Low Temp Phys* 167:108–113, DOI 10.1007/s10909-012-0489-7
- [85] Kunieda Y, Takahashi H, Zen N, Damayanthi R, Mori F, Fujita K, Nakazawa M, Fukuda D, Ohkubo M (2006) Characterization of ir/au pixel tes. *Nuclear Instruments and Methods in Physics Research Section A: Accelerators, Spectrometers, Detectors and Associated Equipment* 559(2):429–431, DOI <https://doi.org/10.1016/j.nima.2005.12.029>, URL <https://www.sciencedirect.com/science/article/pii/S0168900205024204>, proceedings of the 11th International Workshop on Low Temperature Detectors
- [86] van der Kuur J, Gottardi L, Borderias M, Dirks B, de Korte P, Lindeman M, Khosropanah P, den Hartog R, Hoevers H (2011) Small-signal behavior of a TES under ac bias. *IEEE Trans Appl Supercond* 21(3):281–284
- [87] Landau LD, Ginzburg VL (1950) On the theory of superconductivity. *Zh Eksp Teor Fiz* 20:1064, URL <http://cds.cern.ch/record/486430>
- [88] Lee SJ, Adams JS, Bandler SR, Chervenak JA, Eckart ME, Finkbeiner FM, Kelley RL, Kilbourne CA, Porter FS, Sadleir JE, Smith SJ, Wassell EJ (2015) Fine pitch transition-edge sensor X-ray microcalorimeters with sub-eV energy resolution at 1.5 keV. *Applied Physics Letters* 107(22):223503, DOI 10.1063/1.4936793

- [89] Leutenegger MA, Eckart ME, Moseley SJ, Rohrbach SO, Black JK, Chiao MP, Kelley RL, Kilbourne CA, Porter FS (2020) Simple, compact, high-resolution monochromatic x-ray source for characterization of x-ray calorimeter arrays. *Review of Scientific Instruments* 91(8):083110, DOI 10.1063/5.0005206, URL <https://doi.org/10.1063/5.0005206>, <https://doi.org/10.1063/5.0005206>
- [90] Levine MA, Marrs RE, Henderson JR, Knapp DA, Schneider MB (1988) The electron beam ion trap: A new instrument for atomic physics measurements. *Physica Scripta* T22:157–163, DOI 10.1088/0031-8949/1988/t22/024, URL <https://doi.org/10.1088/0031-8949/1988/t22/024>
- [91] Levy S, Lahoud E, Shomroni I, Steinhauer J (2007) The a.c. and d.c. Josephson effects in a Bose-Einstein condensate. *Nature* 449(7162):579–583, DOI 10.1038/nature06186
- [92] Likharev K (1979) *Rev Mod Phys* 51:101
- [93] Likharev K, Semenow V (1972) *SovPhys JEPT Lett* 15:442
- [94] Lindeman MA, Bandler S, Brekosky RP, Chervenak JA, Figueroa-Feliciano E, Finkbeiner FM, Li MJ, Kilbourne CA (2004) Impedance measurements and modeling of a transition-edge-sensor calorimeter. *Rev Sci Instrum* 75(5):1283–1289
- [95] Lindeman MA, Bandler S, Brekosky RP, Chervenak JA, Figueroa-Feliciano E, Finkbeiner FM, Saab T, Stahle CK (2004) Characterization and reduction of noise in mo/au transition edge sensors. *Nuclear Instruments and Methods in Physics Research Section A: Accelerators, Spectrometers, Detectors and Associated Equipment* 520(1):348 – 350, DOI <https://doi.org/10.1016/j.nima.2003.11.264>, URL <http://www.sciencedirect.com/science/article/pii/S0168900203031632>, proceedings of the 10th International Workshop on Low Temperature Detectors
- [96] Lindeman MA, Dirks B, van der Kuur J, de Korte PAJ, den Hartog RH, Gottardi L, Hijmering RA, Hoevers HFC, Khosropanah P (2011) Relationships between complex impedance, thermal response, and noise in tes calorimeters and bolometers. *IEEE Transactions on Applied Superconductivity* 21(3):254–257, DOI 10.1109/TASC.2010.2096173
- [97] Lita AE, Rosenberg D, Nam S, Miller AJ, Balzar D, Kaatz LM, Schwall RE (2005) Tuning of tungsten thin film superconducting transition temperature for fabrication of photon number resolving detectors. *IEEE Transactions on Applied Superconductivity* 15(2):3528–3531, DOI 10.1109/TASC.2005.849033
- [98] Lolli L, Taralli E, Portesi C, Rajteri M, Monticone E (2016) Aluminum–titanium bilayer for near-infrared transition edge sensors. *Sensors* 16(7), DOI 10.3390/s16070953, URL <https://www.mdpi.com/1424-8220/16/7/953>
- [99] Lorenz M, Kirsch C, Merino-Alonso PE, Peille P, Dauser T, Cucchetti E, Smith SJ, Wilms J (2020) GPU Supported Simulation of Transition-Edge Sensor Arrays. *Journal of Low Temperature Physics* 200(5-6):277–285, DOI 10.1007/s10909-020-02450-1
- [100] Lotti S, Macculi C, D’Andrea M, Fioretti V, Dondero P, Mantero A, Minervini G, Argan A, Piro L (2018) Estimates for the background of the ATHENA X-IFU instrument: the cosmic rays contribution. In: den Herder JWA, Nikzad S, Nakazawa K (eds) *Space Telescopes and Instrumentation 2018: Ultraviolet to Gamma Ray*, International Society for Optics and Photonics, SPIE, vol 10699, pp 397 – 405, DOI 10.1117/12.2313236
- [101] Lotti S, D’Andrea M, Molendi S, Macculi C, Minervini G, Fioretti V, Laurenza M, Jacquy C, Piro L (2021) Review of the particle background of the Athena X-IFU instrument. *arXiv e-prints* arXiv:2101.02526, [2101.02526](https://arxiv.org/abs/2101.02526)
- [102] Maasilta IJ (2012) Complex impedance, responsivity and noise of transition-edge sensors: Analytical solutions for two- and three-block thermal models. *AIP Advances* 2(4):042110
- [103] Malnou M, Aumentado J, Vissers MR, Wheeler JD, Hubmayr J, Ullom JN, Gao J (2021) Performance of a Kinetic-Inductance Traveling-Wave Parametric Amplifier at 4 Kelvin: Toward an Alternative to Semiconductor Amplifiers. *arXiv e-prints* arXiv:2110.08142, [2110.08142](https://arxiv.org/abs/2110.08142)
- [104] Mates JAB, Becker DT, Bennett DA, Dober BJ, Gard JD, Hays-Wehle JP, Fowler JW, Hilton GC, Reintsema CD, Schmidt DR, Swetz DS, Vale LR, Ullom JN (2017) Simultaneous readout of 128 x-ray and gamma-ray transition-edge microcalorimeters using microwave squid multiplexing. *Applied Physics Letters* 111(6):062601, DOI 10.1063/1.4986222

- [105] McCammon D (2005) *Thermal Equilibrium Calorimeters – An Introduction*, Springer Berlin Heidelberg, Berlin, Heidelberg, pp 1–34. DOI 10.1007/10933596\_1, URL [https://doi.org/10.1007/10933596\\_1](https://doi.org/10.1007/10933596_1)
- [106] Miniussi AR, Adams JS, Bandler SR, Chervenak JA, Datesman AM, Eckart ME, Ewin AJ, Finkbeiner FM, Kelley RL, Kilbourne CA, Porter FS, Sadleir JE, Sakai K, Smith SJ, Wakeham NA, Wassell EJ, Yoon W (2018) Performance of an x-ray microcalorimeter with a 240  $\mu\text{m}$  absorber and a 50  $\mu\text{m}$  tes bilayer. *J Low Temp Phys* 193(3):337–343
- [107] Miniussi AR, Adams JS, Bandler SR, Beaumont S, Chang MP, Chervenak JA, Finkbeiner FM, Ha JY, Hummatov R, Kelley RL, Kilbourne CA, Porter FS, Sadleir JE, Sakai K, Smith SJ, Wakeham NA, Wassell EJ (2020) Thermal impact of cosmic ray interaction with an x-ray microcalorimeter array. *J Low Temp Phys* 199:45–55
- [108] Morgan KM, Pappas CG, Bennett DA, Gard JD, Hays-Wehle JP, Hilton GC, Reintsema CD, Schmidt DR, Ullom JN, Swetz DS (2017) Dependence of transition width on current and critical current in transition-edge sensors. *Applied Physics Letters* 110(21):212602, DOI 10.1063/1.4984065
- [109] Morgan KM, Becker DT, Bennett DA, Doriese WB, Gard JD, Irwin KD, Lee SJ, Li D, Mates JAB, Pappas CG, Schmidt DR, Titus CJ, Van Winkle DD, Ullom JN, Wessels A, Swetz DS (2019) Use of transition models to design high performance tess for the lcls-ii soft x-ray spectrometer. *IEEE Transactions on Applied Superconductivity* 29(5):1–5, DOI 10.1109/TASC.2019.2903032
- [110] Mori F, Minamikawa Y, Damayanthi RMT, Leman S, Zen N, Ohno M, Takahashi H, Toyokawa H, Tanida H, Uruga T (2008) Synchrotron beam test of a position-sensitive small-pixel ir-tes array. *Journal of Low Temperature Physics* 151(1-2):150–154, DOI {10.1007/s10909-007-9625-1}, 12th International Workshop on Low Temperature Detectors, Paris, FRANCE, JUL 22-27, 2007
- [111] Nagayoshi K, Ridder ML, Bruijn MP, Gottardi L, Taralli E, Khosropanah P, Akamatsu H, Visser S, Gao JR (2020) Development of a Ti/Au TES Microcalorimeter Array as a Backup Sensor for the Athena/X-IFU Instrument. *Journal of Low Temperature Physics* 199:943–948
- [112] Ogorzalek A, Bandler S, Cumbee R, Hodges-Kluck E, Kilbourne C, Leutenegger M, Markevitch M, McCammon D, Porter FS, Ptak A, Sakai K, Smith S, Williams B, Yoon W, Zhang W (2022) Probing physics of galaxy formation with a wide-field X-ray microcalorimeter. In: *AAS/High Energy Astrophysics Division, AAS/High Energy Astrophysics Division*, vol 54, p 108.41
- [113] O’Neil G, Sanders S, Szypryt P, Dipti A Gall, Yang Y, Brewer SM, Doriese R, Fowler J, Naing A, Swetz D, Tan J, Ullom J, Volotka AV, Takacs E, Ralchenko Y (2020) Measurement of the  $^{1/22}\text{P}$ - $^{3/22}\text{P}$  fine-structure splitting in fluorinelike Kr, W, Re, Os, and Ir. *Phys Rev A* 102(3):032803, DOI 10.1103/PhysRevA.102.032803
- [114] O’Neil GC, Szypryt P, Takacs E, Tan JN, Buechele SW, Naing AS, Joe YI, Swetz D, Schmidt DR, Doriese WB, Gard JD, Reintsema CD, Ullom JN, Villarrubia JS, Ralchenko Y (2020) On Low-Energy Tail Distortions in the Detector Response Function of X-Ray Microcalorimeter Spectrometers. *Journal of Low Temperature Physics* 199(3-4):1046–1054, DOI 10.1007/s10909-019-02270-y, 2005.05395
- [115] Orlando A, Ceriale V, Ceruti G, De Gerone M, Faverzani M, Ferri E, Gallucci G, Giachero A, Nucciotti A, Puiu A, Schmidt D, Swetz D, Ullom J (2018) Microfabrication of transition-edge sensor arrays of microcalorimeters with 163ho for direct neutrino mass measurements with holmes. *Journal of Low Temperature Physics* 193, DOI 10.1007/s10909-018-1968-2
- [116] Parra-Borderias M, Fernandez-Martinez I, Fabrega L, Camon A, Gil O, Costa-Kramer JL, Gonzalez-Arrabal R, Sese J, Bueno J, Briones F (2013) Characterization of a Mo/Au Thermometer for ATHENA. *IEEE Transactions on Applied Superconductivity* 23(3):2300405–2300405, DOI 10.1109/TASC.2012.2236140
- [117] Peille P, Dauser T, Kirsch C, den Hartog R, Cucchetti E, Wilms J, Barret D, den Herder JW, Piro L (2018) The Performance of the Athena X-ray Integral Field Unit at Very High Count Rates. *Journal of Low Temperature Physics* 193(5-6):940–948, DOI 10.1007/s10909-018-1964-6
- [118] Peille P, den Hartog R, Miniussi A, Stever S, Bandler S, Kirsch C, Lorenz M, Dauser T, Wilms J, Lotti S, Gatti F, Macculi C, Jackson B, Pajot F (2020) *J Low Temp Phys* 199:240–249
- [119] Porter FS, Audley MD, Beiersdorfer P, Boyce KR, Brekosky RP, Brown GV, Gendreau KC, Gygas JD, Kahn SM, Kelley RL, Stahle CK, Szymkowiak AE (2000) Laboratory astrophysics using a spare XRS microcalorimeter. In: Flanagan KA, Siegmund OHW (eds) *X-Ray and Gamma-Ray*



- Instrumentation for Astronomy XI, International Society for Optics and Photonics, SPIE, vol 4140, pp 407 – 418, DOI 10.1117/12.409137, URL <https://doi.org/10.1117/12.409137>
- [120] Porter FS, Gygax J, Kelley RL, Kilbourne CA, King JM, Beiersdorfer P, Brown GV, Thorn DB, Kahn SM (2008) Performance of the ebit calorimeter spectrometer. *Review of Scientific Instruments* 79(10):10E307, DOI 10.1063/1.2957925, URL <https://doi.org/10.1063/1.2957925>
- [121] Porter FS, Chiao MP, Eckart ME, Fujimoto R, Ishisaki Y, Kelley RL, Kilbourne CA, Leutenegger MA, McCammon D, Mitsuda K, Sawada M, Szymkowiak AE, Takei Y, Tashiro M, Tsujimoto M, Watanabe T, Yamada S (2016) Temporal Gain Correction for X-ray Calorimeter Spectrometers. *Journal of Low Temperature Physics* 184(1-2):498–504, DOI 10.1007/s10909-016-1503-2
- [122] Rothe J, Angloher G, Bauer P, Bento A, Bucci C, Canonica L, D’Addabbo A, Defay X, Erb A, Feilitzsch Fv, Ferreira Iachellini N, Gorla P, Gütlein A, Hauff D, Jochum J, Kiefer M, Kluck H, Kraus H, Lanfranchi JC, Langenkämper A, Loebell J, Mancuso M, Mondragon E, Münster A, Pagliarone C, Petricca F, Potzel W, Pröbst F, Puig R, Reindl F, Schäffner K, Schieck J, Schipperges V, Schönert S, Seidel W, Stahlberg M, Stodolsky L, Strandhagen C, Strauss R, Tanzke A, Trinh Thi HH, Türkoğlu C, Ulrich A, Usharov I, Wawoczny S, Willers M, Wüstrich M (2018) TES-Based Light Detectors for the CRESST Direct Dark Matter Search. *Journal of Low Temperature Physics* 193(5-6):1160–1166, DOI 10.1007/s10909-018-1944-x
- [123] Sadleir J, Smith S, Bandler S, Chervenak J, Clem J (2010) *Phys Rev Lett* 104:047003
- [124] Sadleir JE, Smith SJ, Robinson IK, Finkbeiner FM, Chervenak JA, Bandler SR, Eckart ME, Kilbourne CA (2011) Proximity effects and nonequilibrium superconductivity in transition-edge sensors. *Phys Rev B* 84:184502, DOI 10.1103/PhysRevB.84.184502, URL <https://link.aps.org/doi/10.1103/PhysRevB.84.184502>
- [125] Sadleir JE, Lee SJ, Smith SJ, Busch SE, Bandler SR, Adams JS, Eckart ME, Chervenak JA, Kelley RL, Kilbourne CA, Porter FS, Porst JP (2014) The Magnetically-Tuned Transition-Edge Sensor. *Journal of Low Temperature Physics* 176(3-4):392–399, DOI 10.1007/s10909-014-1194-5
- [126] Sakai K, Adams JS, Bandler SR, Chervenak JA, Datesman AM, Eckart ME, Finkbeiner FM, Kelley RL, Kilbourne CA, Miniussi AR, Porter FS, Sadleir JS, Smith SJ, Wakeham NA, Wassell EJ, Yoon W, Akamatsu H, Bruijn MP, Gottardi L, Jackson BD, van der Kuur J, van Leeuwen BJ, van der Linden AJ, van Weers HJ, Kiviranta M (2018) Study of Dissipative Losses in AC-Biased Mo/Au Bilayer Transition-Edge Sensors. *Journal of Low Temperature Physics* 193(3-4):356–364, DOI 10.1007/s10909-018-2002-4
- [127] Sakai K, Adams J, Bandler SR, Beaumont S, Chervenak J, Datesman A, Finkbeiner F, Kelley R, Kilbourne C, Miniussi A, Porter F, Sadleir J, Smith S, Wakeham N, Wassell E, Eckart M, Ryu K (2019) Demonstration of fine-pitch high resolution x-ray transition-edge sensor microcalorimeters optimized for energies below 1 keV. Presented at the 18th International Workshop on Low Temperature Detectors (LTD 18), Milano, Italy, July 22-26
- [128] Sakai K, Adams JS, Bandler SR, Beaumont S, Chervenak JA, Datesman AM, Finkbeiner FM, Kelley RL, Kilbourne CA, Miniussi AR, Porter FS, Sadleir JE, Smith SJ, Wakeham NA, Wassell EJ, Jaekel FT, McCammon D, Eckart ME, Ryu K (2020) Demonstration of fine-pitch high-resolution x-ray transition-edge sensor microcalorimeters optimized for energies below 1 keV. *J Low Temp Phys* 199:949–954
- [129] Sato K, Ohashi T, Ishisaki Y, Ezoe Y, Yamada S, et al. (2020) Super DIOS mission for exploring “dark baryon”. In: den Herder JWA, Nikzad S, Nakazawa K (eds) *Space Telescopes and Instrumentation 2020: Ultraviolet to Gamma Ray*, International Society for Optics and Photonics, SPIE, vol 11444, pp 960 – 969, DOI 10.1117/12.2561681
- [130] Seta H, Tashiro MS, Ishisaki Y, Tsujimoto M, Shimoda Y, Takeda S, Yamaguchi S, Mitsuda K, Fujimoto R, Takei Y, Kelley RL, Boyce KR, Kilbourne CA, Porter FS, Miko JJ, Masukawa K, Matsuda K (2012) Development of the onboard digital processing system for the soft x-ray spectrometer of ASTRO-H: performance in the engineering model tests. In: Takahashi T, Murray SS, den Herder JWA (eds) *Space Telescopes and Instrumentation 2012: Ultraviolet to Gamma Ray*, International Society for Optics and Photonics, SPIE, vol 8443, pp 1542 – 1551, DOI 10.1117/12.924638, URL <https://doi.org/10.1117/12.924638>

- [131] Shank B, Yen JJ, Cabrera B, Kreikebaum JM, Moffatt R, Redl P, Young BA, Brink PL, Cherry M, Tomada A (2014) Nonlinear optimal filter technique for analyzing energy depositions in TES sensors driven into saturation. *AIP Advances* 4(11):117106, DOI 10.1063/1.4901291, [1406.7030](https://doi.org/10.1063/1.4901291)
- [132] Simionescu A, Ettore S, Werner N, Nagai D, Vazza F, Akamatsu H, Pinto C, de Plaa J, Wijers N, Nelson D, Pointecouteau E, Pratt GW, Spiga D, Lau E, Rossetti M, Gastaldello F, Biffi V, Bulbul E, den Herder JW, Eckert D, Fraternali F, Mingo B, Pareschi G, Pezzulli G, Reiprich TH, Schaye J, Walker SA, Werk J (2019) Voyage through the Hidden Physics of the Cosmic Web. arXiv e-prints arXiv:1908.01778, [1908.01778](https://arxiv.org/abs/1908.01778)
- [133] Smith S, Adams J, Bailey C, Bandler S, Chervenak J, Eckart M, Finkbeiner F, Kelley R, Kilbourne C, Porter F, Sadleir J (2013) *J Appl Phys* 114:074513
- [134] Smith SJ, Whitford C, Fraser GW, Holland AD, Goldie D, R Ashton TJ, Limpenny RJ, Stevenson T (2004) First results from a 1-d imaging spectrometer using ir tess. *Nuclear Instruments and Methods in Physics Research Section A: Accelerators, Spectrometers, Detectors and Associated Equipment* 520(1):449–451, DOI <https://doi.org/10.1016/j.nima.2003.11.369>, URL <https://www.sciencedirect.com/science/article/pii/S0168900203032893>, proceedings of the 10th International Workshop on Low Temperature Detectors
- [135] Smith SJ, Whitford CH, Fraser GW (2006) Optimised filtering for improved energy and position resolution in position-sensitive TES based X-ray detectors. *Nuclear Instruments and Methods in Physics Research A* 556(1):237–245, DOI 10.1016/j.nima.2005.10.021
- [136] Smith SJ, Bandler SR, Brekosky RP, Brown AD, Chervenak JA, Eckart ME, Figueroa-Feliciano E, Finkbeiner FM, Kelley RL, Kilbourne CA, Porter FS, Sadleir JE (2008) Development of arrays of position-sensitive microcalorimeters for Constellation-X. In: Turner MJL, Flanagan KA (eds) *Space Telescopes and Instrumentation 2008: Ultraviolet to Gamma Ray*, International Society for Optics and Photonics, SPIE, vol 7011, pp 645 – 652, DOI 10.1117/12.790100, URL <https://doi.org/10.1117/12.790100>
- [137] Smith SJ, Bandler SR, Brekosky RP, Brown AD, Chervenak JA, Eckart ME, Figueroa-Feliciano E, Finkbeiner FM, Kelley RL, Kilbourne CA, Porter FS, Sadleir JE (2009) Development of position-sensitive transition-edge sensor x-ray detectors. *IEEE Transactions on Applied Superconductivity* 19(3):451–455, DOI 10.1109/TASC.2009.2019557
- [138] Smith SJ, Adams JS, Bailey CN, Bandler SR, Chervenak JA, Eckart ME, Finkbeiner FM, Kelley RL, Kilbourne CA, Porter FS, Sadleir JE (2012) Small Pitch Transition-Edge Sensors with Broadband High Spectral Resolution for Solar Physics. *Journal of Low Temperature Physics* 167(3-4):168–175, DOI 10.1007/s10909-012-0574-y
- [139] Smith SJ, Adams JS, Bandler SR, Busch SE, Chervenak JA, Eckart ME, Finkbeiner FM, Kelley RL, Kilbourne CA, Lee SJ, Porst JP, Porter FS, Sadleir JE (2014) Characterization of Mo/Au Transition-Edge Sensors with Different Geometric Configurations. *Journal of Low Temperature Physics* 176(3-4):356–362, DOI 10.1007/s10909-013-1031-2
- [140] Smith SJ, Adams JS, Bandler SR, Betancourt-Martinez GL, Chervenak JA, Chiao MP, Eckart ME, Finkbeiner FM, Kelley RL, Kilbourne CA, Miniussi AR, Porter FS, Sadleir JE, Sakai K, Wakeham NA, Wassell EJ, Yoon W, Bennett DA, Doriese WB, Fowler JW, Hilton GC, Morgan KM, Pappas CG, Reintsema CN, Swetz DS, Ullom JN, Irwin KD, Akamatsu H, Gottardi L, den Hartog R, Jackson BD, van der Kuur J, Barret D, Peille P (2016) Transition-edge sensor pixel parameter design of the microcalorimeter array for the x-ray integral field unit on Athena. In: den Herder JWA, Takahashi T, Bautz M (eds) *Space Telescopes and Instrumentation 2016: Ultraviolet to Gamma Ray*, International Society for Optics and Photonics, SPIE, vol 9905, pp 772 – 790, DOI 10.1117/12.2231749, URL <https://doi.org/10.1117/12.2231749>
- [141] Smith SJ, Adams JS, Bandler SR, Chervenak JA, Datesman AM, Eckart ME, Finkbeiner FM, Hummatov R, Kelley RL, Kilbourne CA, Miniussi AR, Porter FS, Sadleir JE, Sakai K, Wakeham NA, Wassell EJ (2019) Multiabsorber transition-edge sensors for x-ray astronomy. *Journal of Astronomical Telescopes, Instruments, and Systems* 5(2):1 – 11, DOI 10.1117/1.JATIS.5.2.021008, URL <https://doi.org/10.1117/1.JATIS.5.2.021008>
- [142] Smith SJ, Adams JS, Bandler SR, Beaumont S, Chervenak JA, Datesman AM, Finkbeiner FM, Hummatov R, Kelly RL, Kilbourne CA, Miniussi AR, Porter FS, Sadleir JE, Sakai K, Wakeham

- NA, Wassell EJ, Witthoef MC, Ryu K (2020) Toward 100,000-pixel microcalorimeter arrays using multi-absorber transition-edge sensors. *J Low Temp Phys* 199:330–338
- [143] Smith SJ, Adams JS, Bandler SR, Beaumont S, Chervenak JA, Denison EV, Doriese WB, Durkin M, Finkbeiner FM, Fowler JW, Hilton GC, Hummatov R, Irwin KD, Kelley RL, Kilbourne CA, Leutenegger MA, Miniussi AR, Porter FS, Reintsema CD, Sadleir JE, Sakai K, Swetz DS, Ullom JN, Vale LR, Wakeham NA, Wassell EJ, Witthoef MC (2021) Performance of a Broad-Band, High-Resolution, Transition-Edge Sensor Spectrometer for X-ray Astrophysics. *IEEE Transactions on Applied Superconductivity* 31(5):3061918, DOI 10.1109/TASC.2021.3061918
- [144] Stahle CK, Lindeman MA, Figueroa-Feliciano E, Li MJ, Tralshawala N, Finkbeiner FM, Brekosky RP, Chervenak JA (2002) Arraying compact pixels of transition-edge microcalorimeters for imaging x-ray spectroscopy. In: Porter FS, McCammon D, Galeazzi M, Stahle CK (eds) *Low Temperature Detectors*, American Institute of Physics Conference Series, vol 605, pp 223–226, DOI 10.1063/1.1457633
- [145] Stern RA, Rausch A, Deiker S, Martínez-Galarce D, Shing L, Irwin KD, Ullom JN, O’Neil G, Hilton G, Vale L (2008) X-ray Microcalorimeter Research for Solar Physics at LMSAL and NIST: An Update. *Journal of Low Temperature Physics* 151(3-4):721–726, DOI 10.1007/s10909-008-9735-4
- [146] Szymkowiak AE, Kelley RL, Moseley SH, Stahle CK (1993) Signal processing for microcalorimeters. *Journal of Low Temperature Physics* 93(3-4):281–285, DOI 10.1007/BF00693433
- [147] Szypryt P, O’Neil GC, Takacs E, Tan JN, Buechele SW, Naing AS, Bennett DA, Doriese WB, Durkin M, Fowler JW, Gard JD, Hilton GC, Morgan KM, Reintsema CD, Schmidt DR, Swetz DS, Ullom JN, Ralchenko Y (2019) A transition-edge sensor-based x-ray spectrometer for the study of highly charged ions at the national institute of standards and technology electron beam ion trap. *Review of Scientific Instruments* 90(12):123107, DOI 10.1063/1.5116717, URL <https://doi.org/10.1063/1.5116717>, <https://doi.org/10.1063/1.5116717>
- [148] Takahashi T, Kokubun M, Mitsuda K, Kelley RL, Ohashi T, Aharonian F, Akamatsu H, Akimoto F, Allen SW, Anabuki N, Angelini L, Arnaud K, Asai M, Audard M, Awaki H, Axelsson M, Azzarello P, Baluta C, Bamba A, Bando N, Bautz MW, Bialas T, Blandford R, Boyce K, Brenneman LW, Brown GV, Bulbul E, Cackett EM, Canavan E, Chernyakova M, Chiao MP, Coppi PS, Costantini E, O’Dell S, DiPirro M, Done C, Dotani T, Doty J, Ebisawa K, Eckart ME, Enoto T, Ezoe Y, Fabian AC, Ferrigno C, Foster AR, Fujimoto R, Fukazawa Y, Funk S, Furuzawa A, Galeazzi M, Gallo LC, Gandhi P, Gilmore K, Giustini M, Goldwurm A, Gu L, Guainazzi M, Haas D, Haba Y, Hagino K, Hamaguchi K, Harrus IM, Hatsukade I, Hayashi T, Hayashi K, Hayashida K, den Herder JW, Hiraga JS, Hirose K, Hornschemeier A, Hoshino A, Hughes JP, Ichinohe Y, Iizuka R, Inoue H, Inoue Y, Ishibashi K, Ishida M, Ishikawa K, Ishimura K, Ishisaki Y, Itoh M, Iwai M, Iwata N, Iyomoto N, Jewell C, Kaastra J, Kallman T, Kamae T, Kara E, Kataoka J, Katsuda S, Katsuta J, Kawaharada M, Kawai N, Kawano T, Kawasaki S, Khangulyan D, Kilbourne CA, Kimball M, King A, Kitaguchi T, Kitamoto S, Kitayama T, Kohmura T, Konami S, Kosaka T, Koujelev A, Koyama K, Koyama S, Kretschmar P, Krimm HA, Kubota A, Kunieda H, Laurent P, Lee SH, Leutenegger MA, Limousin O, Loewenstein M, Long KS, Lumb D, Madejski G, Maeda Y, Maier D, Makishima K, Markevitch M, Masters C, Matsumoto H, Matsushita K, McCammon D, Mcguinness D, McNamara BR, Mehdipour M, Miko J, Miller ED, Miller JM, Mineshige S, Minesugi K, Mitsuishi I, Miyazawa T, Mizuno T, Mori H, Mori K, Moroso F, Moseley H, Muench T, Mukai K, Murakami H, Murakami T, Mushotzky RF, Nagano H, Nagino R, Nakagawa T, Nakajima H, Nakamori T, Nakano T, Nakashima S, Nakazawa K, Namba Y, Natsukari C, Nishioka Y, Nobukawa KK, Nobukawa M, Noda H, Nomachi M, Odaka H, Ogawa H, Ogawa M, Ogi K, Ohno M, Ohta M, Okajima T, Okamoto A, Okazaki T, Ota N, Ozaki M, Paerels F, Paltani S, Parmar A, Petre R, Pinto C, de Plaa J, Pohl M, Pontius J, Porter FS, Pottschmidt K, Ramsey B, Reynolds C, Russell H, Safi-Harb S, Saito S, Sakai K, Sakai Si, Sameshima H, Sasaki T, Sato G, Sato K, Sato R, Sato Y, Sawada M, Schartel N, Serlemitsos PJ, Seta H, Shibano Y, Shida M, Shidatsu M, Shimada T, Shinozaki K, Shirron P, Simionescu A, Simmons C, Smith RK, Sneiderman G, Soong Y, Stawarz Ł, Sugawara Y, Sugita S, Sugita H, Szymkowiak A, Tajima H, Takahashi H, Takeda S, Takei Y, Tamagawa T, Tamura T, Tamura K, Tanaka T, Tanaka Y, Tanaka YT, Tashiro MS, Tawara Y, Terada Y, Terashima Y, Tombesi F, Tomida H, Tsuboi Y, Tsujimoto M, Tsunemi H, Tsuru TG, Uchida H, Uchiyama H, Uchiyama Y, Ueda S, Ueda Y, Ueno S, Uno S, Urry CM, Ursino E, de Vries CP, Wada A, Watanabe S, Watanabe T, Werner N, Wik DR, Wilkins

- DR, Williams BJ, Yamada S, Yamada T, Yamaguchi H, Yamaoka K, Yamasaki NY, Yamauchi M, Yamauchi S, Yaqoob T, Yatsu Y, Yonetoku D, Yoshida A, Yuasa T, Zhuravleva I, Zoghbi A (2018) Hitomi (ASTRO-H) X-ray Astronomy Satellite. *Journal of Astronomical Telescopes, Instruments, and Systems* 4:021402, DOI 10.1117/1.JATIS.4.2.021402
- [149] Takeda S, Tashiro MS, Ishisaki Y, Tsujimoto M, Seta H, Shimoda Y, Yamaguchi S, Uehara S, Terada Y, Fujimoto R, Mitsuda K (2014) Performance verification and system integration tests of the pulse shape processor for the soft x-ray spectrometer onboard ASTRO-H. In: Takahashi T, den Herder JWA, Bautz M (eds) *Space Telescopes and Instrumentation 2014: Ultraviolet to Gamma Ray*, Society of Photo-Optical Instrumentation Engineers (SPIE) Conference Series, vol 9144, p 91445B, DOI 10.1117/12.2055899
- [150] Takei Y, Gottardi L, Hoevers H, de Korte AJ, van der Kuur J, Ridder ML, Bruijn MP (2008) Characterization of a high-performance ti/au tes microcalorimeter with a central cu absorber. *J Low Temp Phys* 151:161–166
- [151] Taralli E, Khosropanah P, Gottardi L, Nagayoshi K, Ridder ML, Bruijn MP, Gao JR (2019) Complex impedance of tess under ac bias using fdm readout system. *AIP Advances* 9(4):045324
- [152] Tolpygo SK, Bolkhovskiy V, Weir TJ, Johnson LM, Gouker MA, Oliver WD (2015) Fabrication Process and Properties of Fully-Planarized Deep-Submicron Nb/Al- $\text{AlO}_x$ /Nb Josephson Junctions for VLSI Circuits. *IEEE Transactions on Applied Superconductivity* 25(3):2374836, DOI 10.1109/TASC.2014.2374836, [1408.5829](https://doi.org/10.1109/TASC.2014.2374836)
- [153] Tsujimoto M, Tashiro MS, Ishisaki Y, Yamada S, Seta H, Mitsuda K, Boyce KR, Eckart ME, Kilbourne CA, Leutenegger MA, Porter FS, Kelley RL (2018) In-Orbit Performance of the Digital Electronics for the X-Ray Microcalorimeter Onboard the Hitomi Satellite. *Journal of Low Temperature Physics* 193(3-4):505–511, DOI 10.1007/s10909-018-1861-z
- [154] Ullom J, Doriese W, Hilton G, Beall J, Deiker S, Irwin K, Reintsema C, Vale L, Xu Y (2004) Suppression of excess noise in transition-edge sensors using magnetic field and geometry. *Nucl Instrum Methods A* 520(1):333 – 335
- [155] Ullom JN, Bennett DA (2015) Review of superconducting transition-edge sensors for x-ray and gamma-ray spectroscopy. *Superconductor Science and Technology* 28(8):084003, DOI 10.1088/0953-2048/28/8/084003
- [156] Vaccaro D, Akamatsu H, Gottardi L, van der Kuur J, Taralli E, de Wit M, Bruijn MP, den Hartog R, Kiviranta M, van der Linden AJ, Nagayoshi K, Ravensberg K, Ridder ML, Visser S, Jackson BD, Gao JR, Hoogeveen RWM, den Herder JWA (2022) Susceptibility study of TES micro-calorimeters for X-ray spectroscopy under FDM readout. *arXiv e-prints arXiv:2208.10875*, [2208.10875](https://arxiv.org/abs/2208.10875)
- [157] de Vries CP, Haas D, Yamasaki NY, den Herder JW, Paltani S, Kilbourne C, Tsujimoto M, Eckart ME, Leutenegger MA, Costantini E, Dercksen JPC, Dubbeldam L, Frericks M, Laubert PP, van Loon S, Lowes P, McCalden AJ, Porter FS, Ruijter J, Wolfs R (2017) Calibration sources and filters of the soft x-ray spectrometer instrument on the Hitomi spacecraft. *Journal of Astronomical Telescopes, Instruments, and Systems* 4(1):1 – 9, DOI 10.1117/1.JATIS.4.1.011204, URL <https://doi.org/10.1117/1.JATIS.4.1.011204>
- [158] Vystavkin A, Gubankov V, Kuzmin L, Likharev K, Migulin V, Semenov V (1974) S-c-s junctions as nonlinear elements of microwave receiving devices. *Rev Phys Appl* 9(1):79–109
- [159] Wakeham NA, Adams JS, Bandler SR, Chervenak JA, Datesman AM, Eckart ME, Finkbeiner FM, Kelley RL, Kilbourne CA, Miniussi AR, Porter FS, Sadleir JE, Sakai K, Smith SJ, Wassell EJ, Yoon W (2018) Effects of normal metal features on superconducting transition-edge sensors. *J Low Temp Phys* 193:231–240
- [160] Wakeham NA, Adams JS, Bandler SR, Beaumont S, Chervenak JA, Datesman AM, Eckart ME, Finkbeiner FM, Hummatov R, Kelley RL, Kilbourne CA, Miniussi AR, Porter FS, Sadleir JE, Sakai K, Smith SJ, Wassell EJ (2019) Thermal fluctuation noise in mo/au superconducting transition-edge sensor microcalorimeters. *J Appl Phys* 125(16):164503
- [161] Wakeham NA, Adams JS, Bandler SR, Beaumont S, Chervenak JA, Datesman AM, Eckart ME, Finkbeiner FM, Hummatov R, Kelley RL, Kilbourne CA, Miniussi AR, Porter FS, Sadleir JE, Sakai K, Smith SJ, Wassell EJ (2020) High-frequency noise peaks in moau superconducting tes microcalorimeters. *J Low Temp Phys* 200:192–196

- [162] Wassell EJ, Adams JS, Bandler SR, Betancourt-Martinez GL, Chiao MP, Chang MP, Chervenak JA, Datesman AM, Eckart ME, Ewin AJ, Finkbeiner FM, Ha JY, Kelley R, Kilbourne CA, Miniussi AR, Sakai K, Porter FS, Sadleir JE, Smith SJ, Wakeham NA, Yoon W (2017) Fabrication of X-Ray Microcalorimeter Focal Planes Composed of Two Distinct Pixel Types. *IEEE Transactions on Applied Superconductivity* 27(4):2633783, DOI 10.1109/TASC.2016.2633783
- [163] van Weers H, et al. (2020) The X-IFU focal plane assembly development model integration and first test results. In: den Herder JWA, Nikzad S, Nakazawa K (eds) *Space Telescopes and Instrumentation 2020: Ultraviolet to Gamma Ray*, International Society for Optics and Photonics, SPIE, vol 11444, DOI 10.1117/12.2563464, URL <https://doi.org/10.1117/12.2563464>
- [164] Wellstood FC, Urbina C, Clarke J (1994) Hot-electron effects in metals. *Phys Rev B* 49(9):5942–5955, DOI 10.1103/PhysRevB.49.5942
- [165] Wessel A, Morgan K, Becker D, Gard J, Hilton G, Mates J, Reintsema C, Schmidt D DR Swetz, Ullom J, et al. (????) arXiv:190711343
- [166] Wessels A, Morgan K, Gard JD, Hilton GC, Mates JAB, Reintsema CD, Schmidt DR, Swetz DS, Ullom JN, Vale LR, Bennett DA (2021) A model for excess Johnson noise in superconducting transition-edge sensors. *Applied Physics Letters* 118(20):202601, DOI 10.1063/5.0043369
- [167] Whitford CH (2005) Implementation of optimal filters for pulse height measurement from non-linear detectors with non-stationary noise. *Nuclear Instruments and Methods in Physics Research Section A: Accelerators, Spectrometers, Detectors and Associated Equipment* 555(1):255–259, DOI <https://doi.org/10.1016/j.nima.2005.09.001>, URL <https://www.sciencedirect.com/science/article/pii/S0168900205018048>
- [168] Wilms J, Smith SJ, Peille P, Ceballos MT, Cobo B, Dauser T, Brand T, den Hartog RH, Bandler SR, de Plaa J, den Herder JWA (2016) TESSIM: a simulator for the Athena-X-IFU. In: den Herder JWA, Takahashi T, Bautz M (eds) *Space Telescopes and Instrumentation 2016: Ultraviolet to Gamma Ray*, International Society for Optics and Photonics, SPIE, vol 9905, pp 1795 – 1801, DOI 10.1117/12.2234435, URL <https://doi.org/10.1117/12.2234435>
- [169] de Wit M, Gottardi L, Taralli E, Nagayoshi K, Ridder ML, Akamatsu H, Bruijn MP, D’Andrea M, van der Kuur J, Ravensberg K, Vaccaro D, Visser S, Gao JR, den Herder JWA (2020) High aspect ratio transition edge sensors for x-ray spectrometry. *J Appl Phys* 128(22):224501
- [170] Yan D, Divan R, Gades LM, Kenesei P, Madden TJ, Miceli A, Park JS, Patel UM, Quaranta O, Sharma H, Bennett DA, Doriese WB, Fowler JW, Gard JD, Hays-Wehle JP, Morgan KM, Schmidt DR, Swetz DS, Ullom JN (2017) Eliminating the non-Gaussian spectral response of X-ray absorbers for transition-edge sensors. *Applied Physics Letters* 111(1):192602, DOI 10.1063/1.5001198
- [171] Yohannes DT, Hunt RT, Vivalda JA, Amparo D, Cohen A, Vernik IV, Kirichenko AF (2015) Planarized, Extendible, Multilayer Fabrication Process for Superconducting Electronics. *IEEE Transactions on Applied Superconductivity* 25(3):2365562, DOI 10.1109/TASC.2014.2365562
- [172] Yoon W, Adams JS, Bandler SR, Betancourt-Martinez GL, Chiao MP, Chang MP, Chervenak JA, Datesman A, Eckart ME, Ewin AJ, Finkbeiner FM, Ha JY, Kelley R, Kilbourne CA, Miniussi AR, Porter FS, Sadleir JE, Sakai K, Smith SJ, Wakeham NA, Wassell E (2017) Design and Performance of Hybrid Arrays of Mo/Au Bilayer Transition-Edge Sensors. *IEEE Transactions on Applied Superconductivity* 27(4):2655718, DOI 10.1109/TASC.2017.2655718
- [173] Zhang S, Eckart ME, Jaeckel FT, Kripps KL, McCammon D, Morgan KM, Zhou Y (2017) Mapping of the resistance of a superconducting transition edge sensor as a function of temperature, current, and applied magnetic field. *Journal of Applied Physics* 121(7):074503, DOI 10.1063/1.4976562
- [174] Zhang X, Duff SM, Hilton GC, Lowell PJ, Morgan KM, Schmidt DR, Ullom JN (2019) Controlling the thermal conductance of silicon nitride membranes at 100 mK temperatures with patterned metal features. *Applied Physics Letters* 115(5):052601, DOI 10.1063/1.5097173